 DOI: 10.1086/695704

Appendix from W. S. Wolbach et al., "Extraordinary Biomass-Burning Episode and Impact Winter Triggered by the Younger Dryas Cosmic Impact ~12,800 Years Ago. 2. Lake, Marine, and Terrestrial Sediments"
(J. Geol., vol. 126, no. 2, p. 000)

Supplemental Material

Supplemental Figures

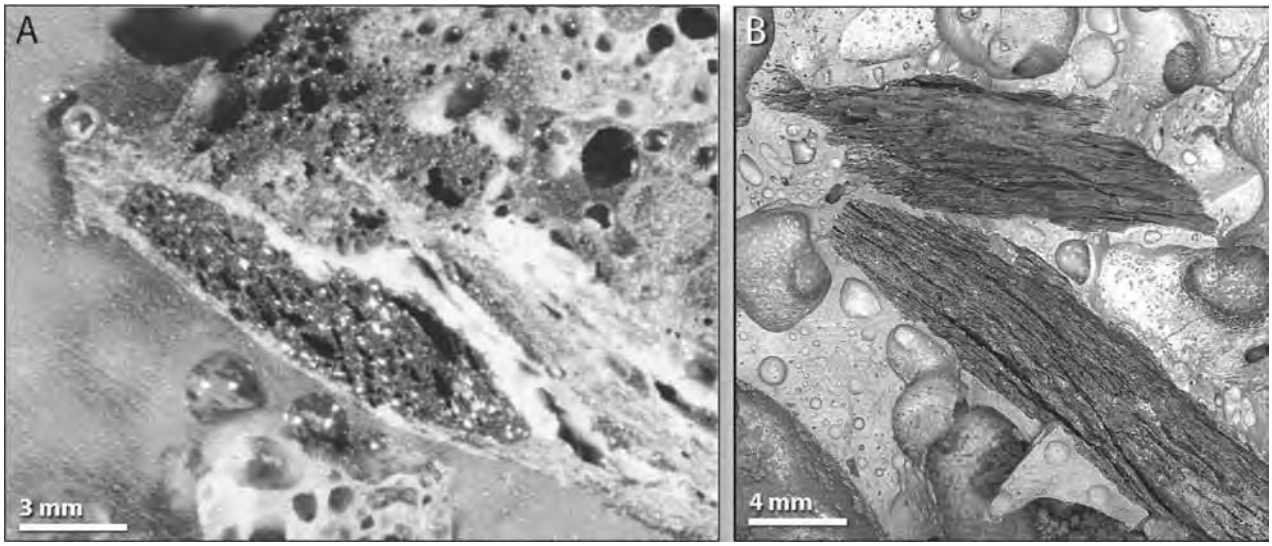

Figure A1. Younger Dryas boundary (YDB) charcoal and meltglass. *A*, SEM image of dark, vesicular charcoal/organic material embedded in YDB meltglass from Melrose, Pennsylvania. *B*, SEM image of charcoal in YDB meltglass from Blackville Bay, South Carolina (Firestone et al. 2007). The melting temperature of aluminosilicate glass is >1200°C, a temperature higher than that of nearly all known wildfires (Bunch et al. 2012), as reflected by the lack of any reports of meltglass associated with wildfires.

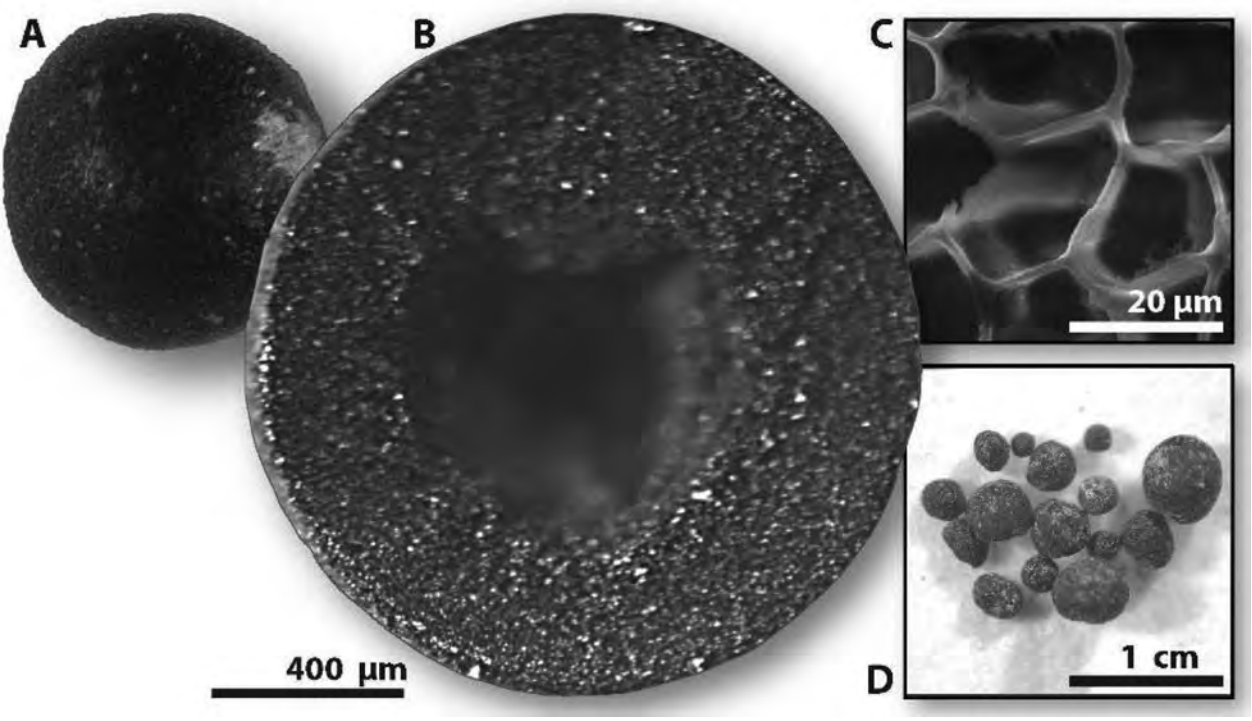

Figure A2. Younger Dryas boundary (YDB) carbon spherules (CSs). *A–C*, Photomicrographs of a whole CS (*A*) and a bisected CS (*B*) and an SEM image of vesicular interior of a CS (*C*), from the YDB layer in a Carolina Bay, southwest of Fayetteville, North Carolina (Firestone et al. 2007). *D*, Photo of a group of CSs from the same site.

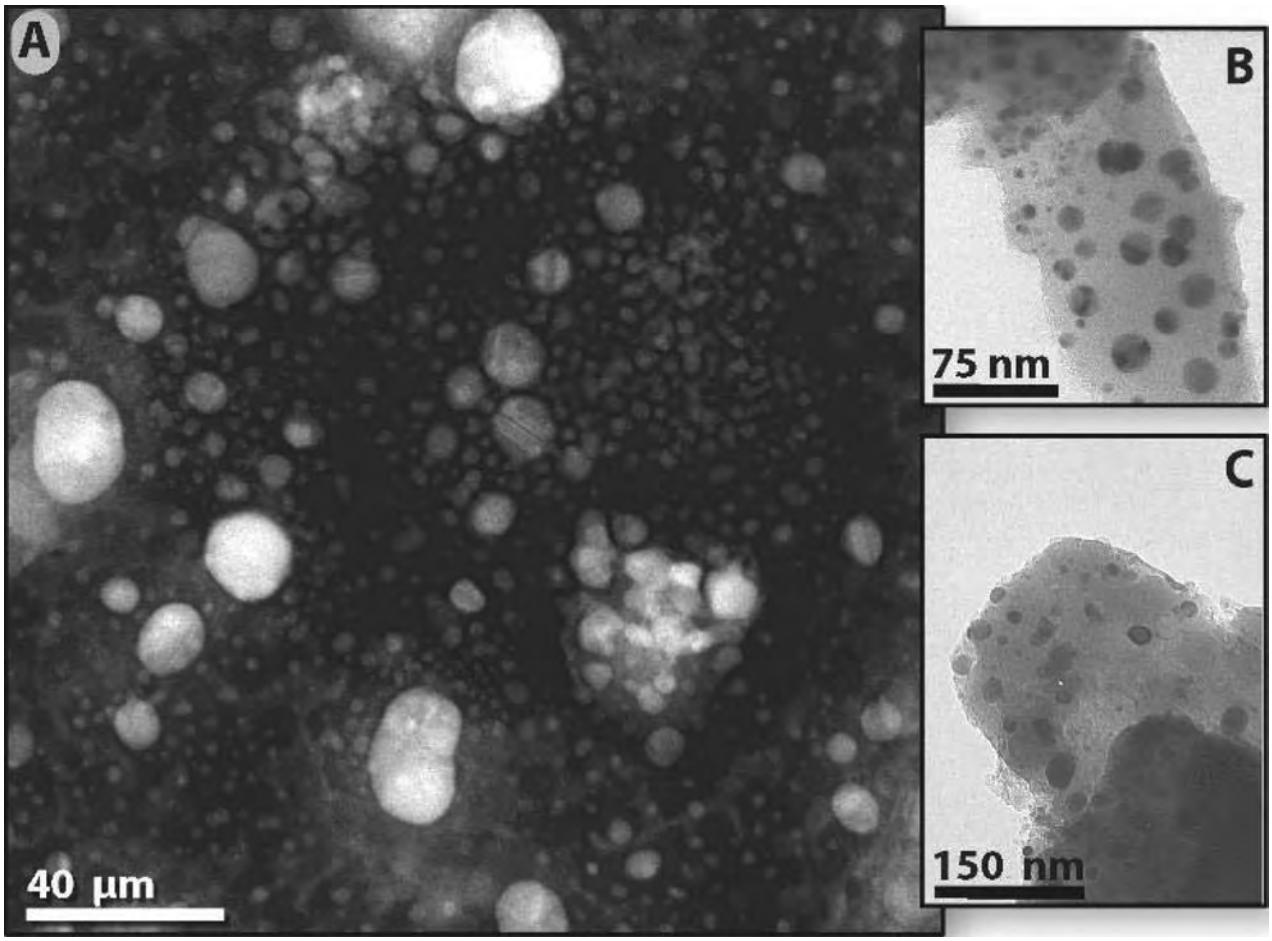

Figure A3. Younger Dryas boundary (YDB) nanodiamonds. *A*, Nanodiamonds from the margin of the Greenland ice sheet near Kangerlussuaq (Kurbatov et al. 2010). *B*, Nanodiamonds in the interior of a carbon spherule from Lommel, Belgium (Kinzie et al. 2014). *C*, Nanodiamonds embedded in matrix of YDB carbon spherules from Kimbel Bay, North Carolina (Kinzie et al. 2014).

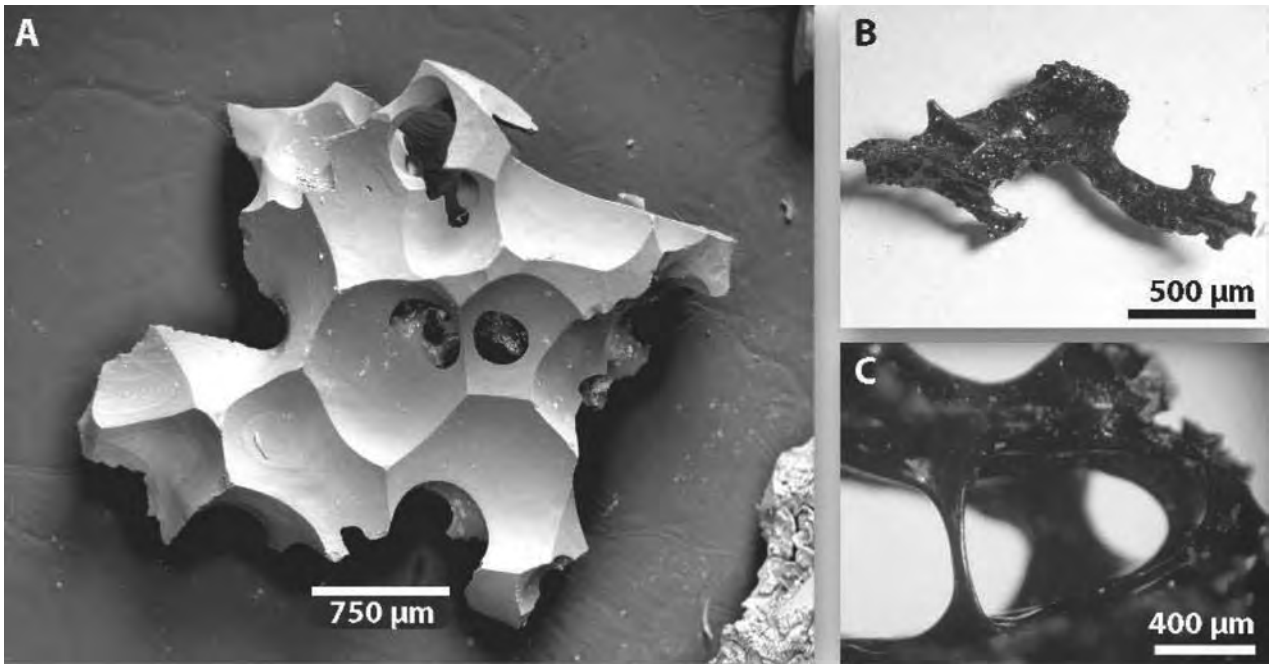

Figure A4. Younger Dryas boundary (YDB) glass-like carbon (GLC). All images are from the M33 site at Myrtle Beach, South Carolina (Firestone et al. 2007). *A*, SEM image of fragment of GLC. *B*, *C*, Photographs of delicate, strand-like GLC.

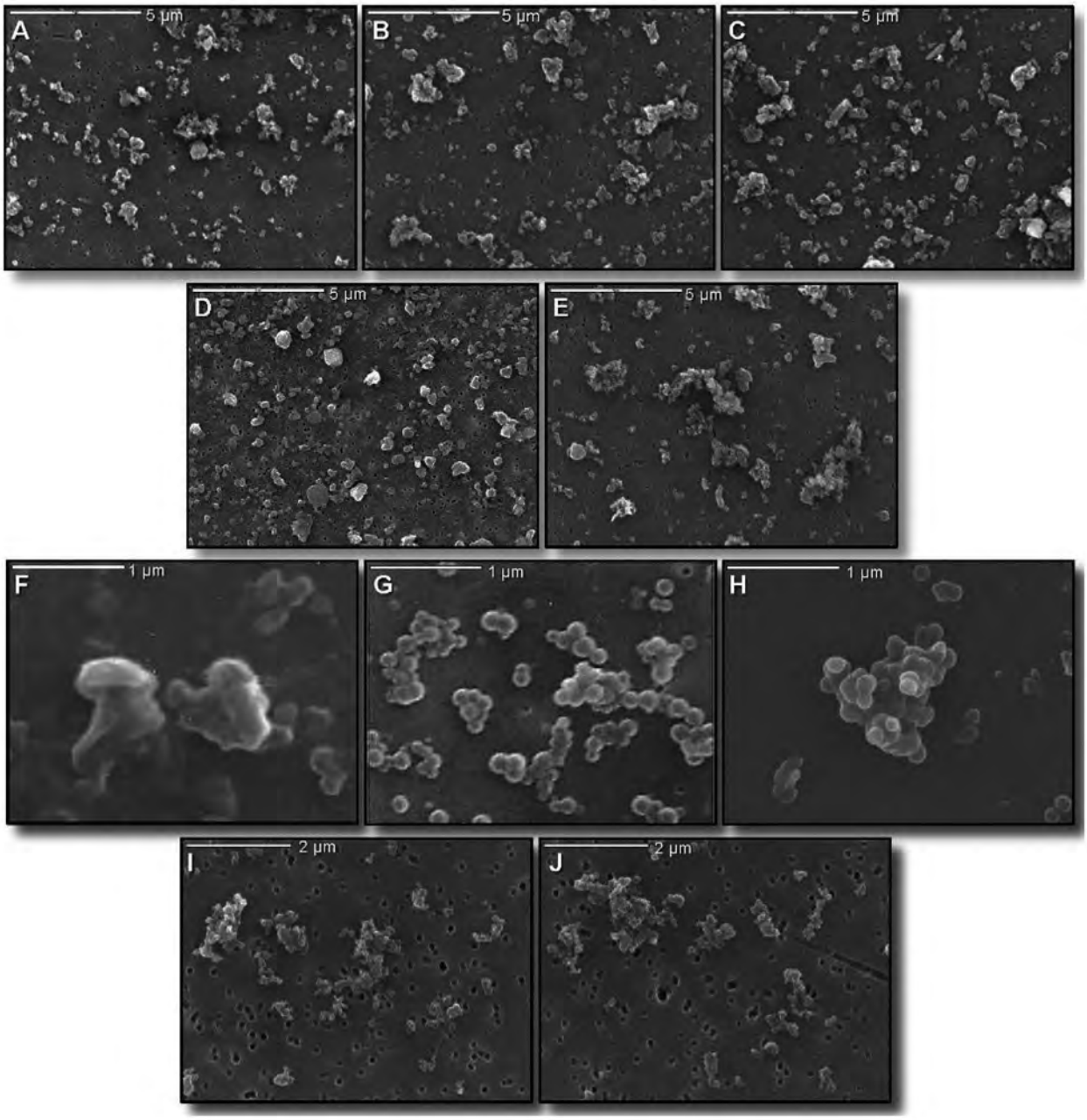

Figure A5. SEM images of aciniform carbon (AC/soot) and black carbon. *A–E*, AC/soot from the Younger Dryas boundary impact layer at Murray Springs, Arizona (*A*), Arlington Canyon, California (*B*), Bull Creek, Oklahoma (*C*), Blackville, South Carolina (*D*), and Halls Cave, Texas (*E*). *F*, Preoxidation carbonaceous residue from the 66 Ma Cretaceous-Tertiary (K-Pg) impact boundary layer at Woodside Creek, New Zealand (Wolbach and Anders 1989). *G*, The same carbonaceous residue from the K-Pg impact boundary layer at Woodside Creek, New Zealand, after 60 h of dichromate oxidation to remove kerogen. The characteristic "grape-bunch" structure of AC/soot, initially masked by a kerogen film, becomes clearly visible after oxidation (Wolbach and Anders 1989). *H*, Processed K-Pg AC/soot from Agost, Spain (Kring and Durda 2003). *I*, *J*, Cabot Corporation's Monarch 120 carbon black, unoxidized.

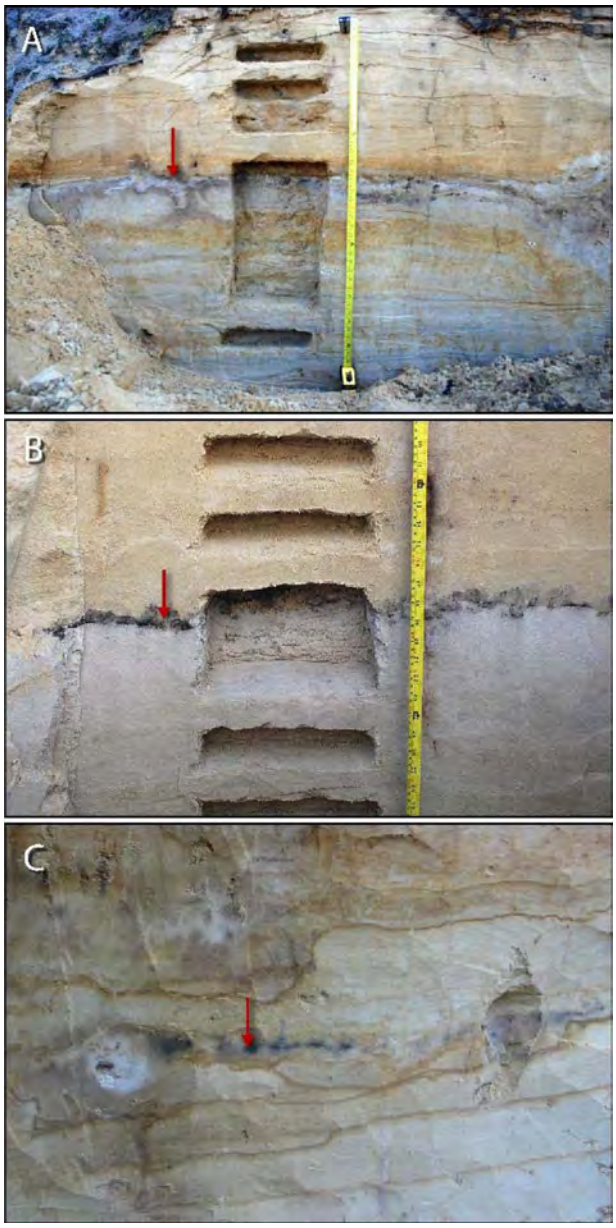

Figure A6. Photographic examples of black mats in northwest Europe. Charcoal-rich black layers (arrows), or "black mats," lie at the boundary between the underlying Usselo Formation and overlying sandy sediment. This layer marks the onset of the Younger Dryas climate episode and precisely coincides with the impact-proxy-rich Younger Dryas boundary layer. Lingen, Germany (*A*), Lommel, Belgium (*B*), and Ommen, Netherlands (*C*), display the black-mat layer at the arrows, with other dark layers above and below that are not impact related.

Figure A7. Locations exhibiting Younger Dryas boundary (YDB) Pt peaks. Twenty-six of the 30 YDB sites display peaks in Pt concentrations: 4 of 8 in this study and 22 previously studied sites for North America, Europe, and Asia. One site is in Greenland (Petaev et al. 2013*b*), one in Russia (Andronikov et al. 2014), four in Lithuania (Andronikov et al. 2015), one on the French-Italian border (Mahaney et al. 2016*b*), three in the Netherlands (Andronikov et al. 2016*b*), two in Belgium (Andronikov et al. 2016*b*), one in the United Kingdom (this study), one in Germany (this study), and 16 in the United States (Andronikov and Andronikova 2016; Moore et al. 2017; this study).

Figure A8. Locations for lake and marine cores with charcoal records used in this investigation. Black circles represent locations of 129 lake cores exhibiting charcoal records that span the Younger Dryas (YD) onset. Purple circles represent marine sites with charcoal and/or soot spanning the YD onset.

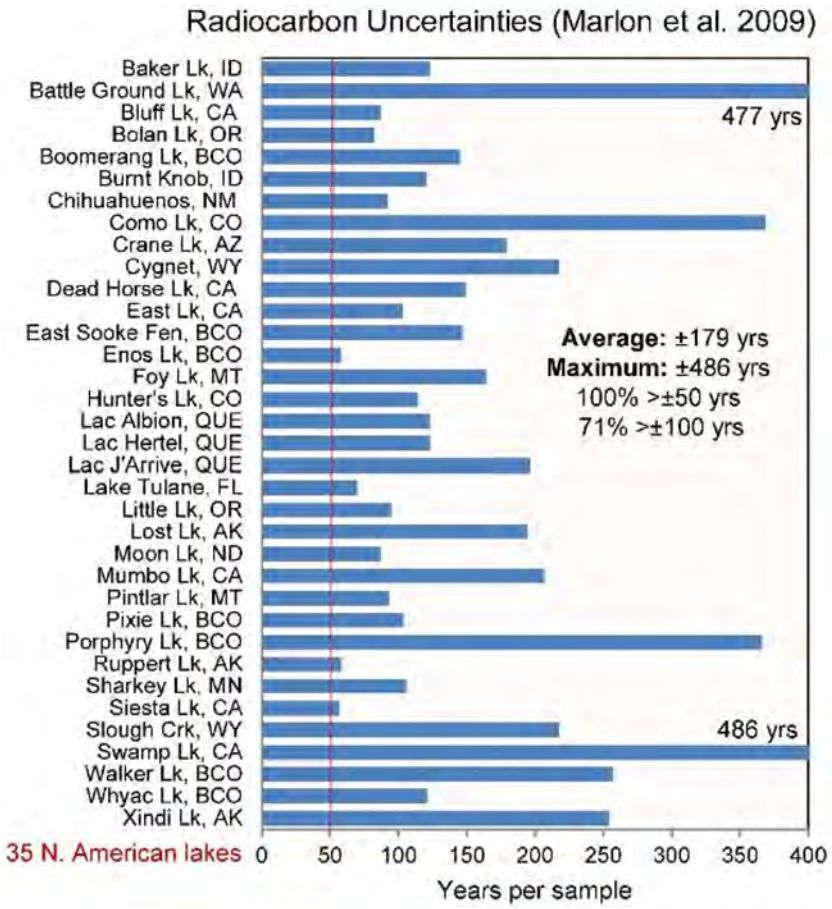

Figure A9. Radiocarbon uncertainties for the 35 lake cores in Marlon et al. (2009). Using the previously published age scales, we selected the ^{14}C date closest to the age of the Younger Dryas boundary layer (Firestone et al. 2007). The average uncertainty is ± 179 y. Uncertainties for all of the 35 lakes are >50 y (red line), refuting a precision of ± 50 y claimed by Marlon et al. (2009). BCO = British Columbia; QUE = Quebec; other abbreviations are for US states.

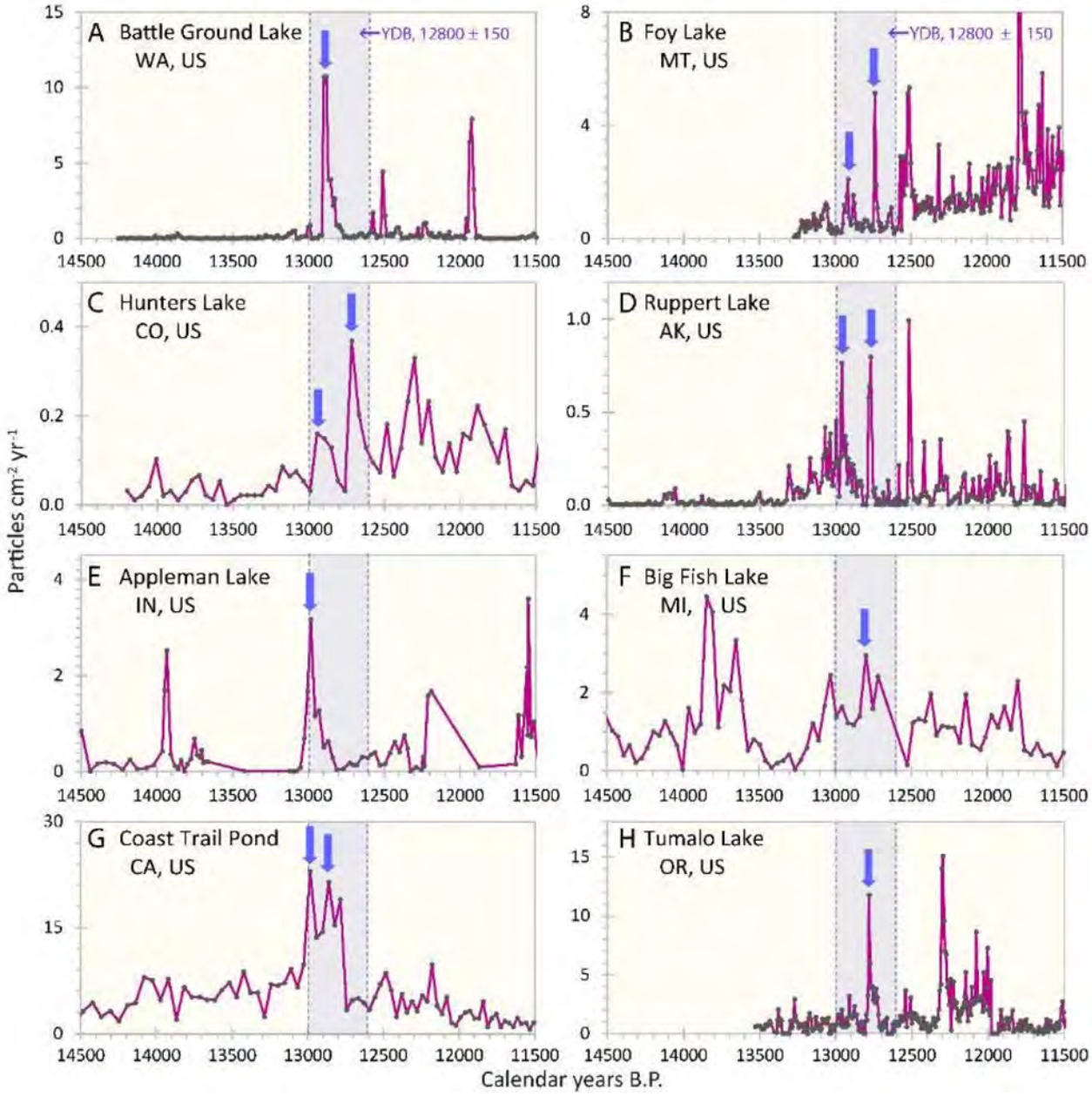

Figure A10. Charcoal records for eight widely distributed lake cores across a 3000-y interval. These raw charcoal North American lake records were selected from among the clearest examples of high charcoal peaks in the 3000-y record (table A9). The vertical bar represents the age range of 12,800 ± 200 cal BP. The range of ±200 y matches the average uncertainty of the dates. All show charcoal peaks in the Younger Dryas (YD) bin (blue arrows) that are the highest or among the highest in the record shown; others show multiple wildfire episodes across the YD interval, any of which could be impact related. Most lakes show multiple charcoal peaks across the interval that includes the YD onset, but not all of those, obviously, are potentially impact related. Although some lakes lack charcoal peaks across the YD interval, there is no requirement that impact-related YD boundary (YDB) wildfires were ubiquitous. Charcoal flux values on the *Y*-axis are in particles/cm^2/y. *A–D*, Four lake cores analyzed by Marlon et al. (2009). *E–H*, Four lake cores in this study. For plots of 35 North American lake-core records, see figures S2 and S3 in Marlon et al. (2009).

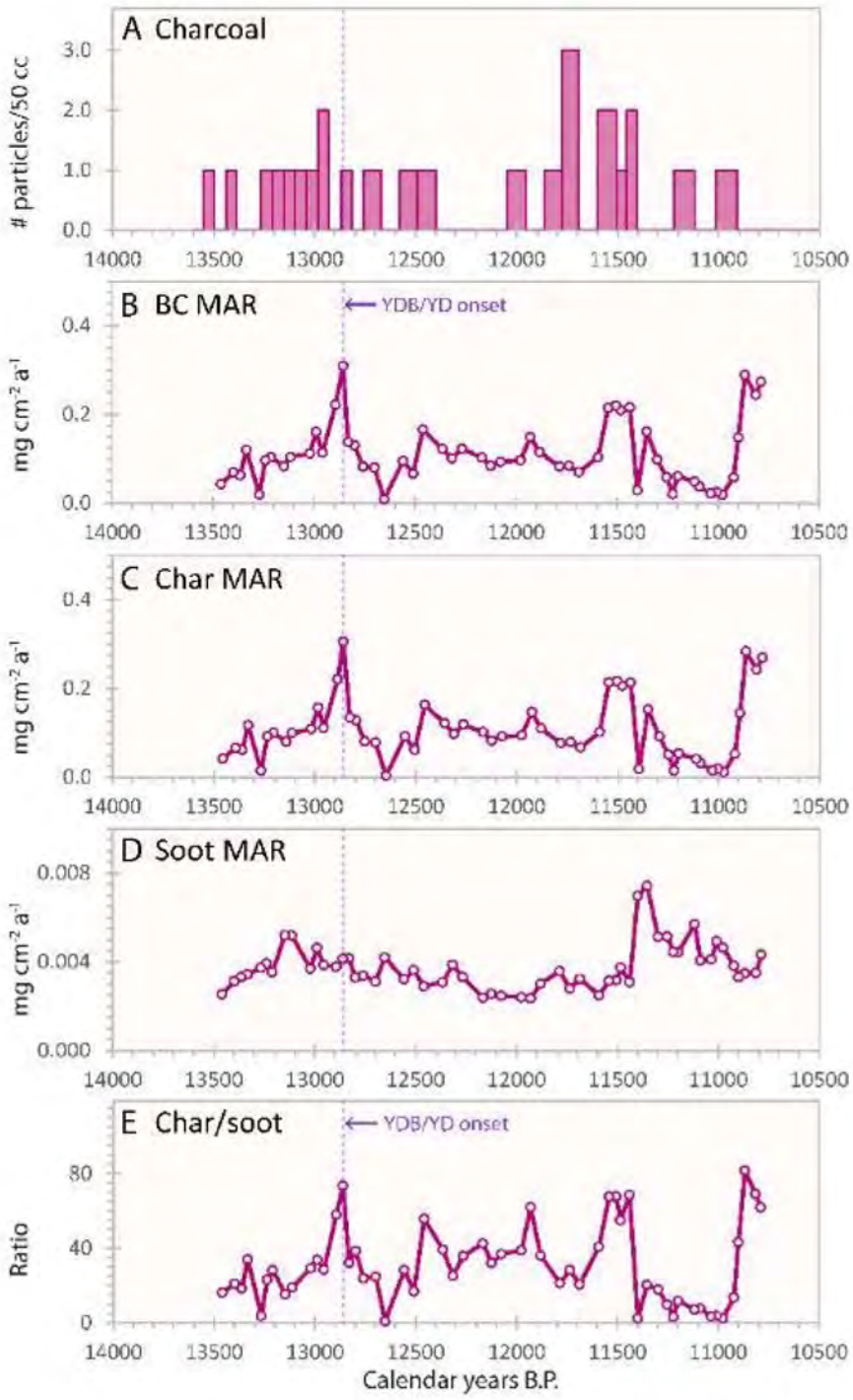

Figure A11. Young Dryas boundary (YDB) biomass-burning indicators at Linsley Pond, Connecticut. An independent group, Han et al. (2016), noted that anomalously high peaks in wildfire proxies in Linsley Pond occurred at 12,800 cal BP (vertical dashed line). The record includes charcoal, black carbon (BC), char, and soot. The BC is produced from the incomplete combustion of biomass and fossil fuels, and it includes both char and soot (Han et al. 2016). Han defines char as a carbon-rich combustion residue formed directly by pyrolysis in smoldering fires, while soot is defined as a combustion condensate produced by gas-to-particle conversion at relatively high temperatures (>600°C) in flame (Han et al. 2016). Three of the highest peaks from the pond fall within the published YDB range of

12,800 ± 150 cal BP. *A*, The charcoal record, an indicator of local fires, shows a peak in charcoal near the Younger Dryas (YD) onset. *B*, Total BC mass accumulation rate (MAR) shows the highest peak in the record at the YDB, suggesting that there was intense regional fire activity, corresponding to the peak in local fires shown in *A*. *C*, Char MAR shows a high YDB peak, also suggesting regional fire activity. *D*, There is no YDB soot peak. Because all wildfires produce both charcoal and soot simultaneously, the presence of a significant YDB charcoal peak at this site with no corresponding soot peak suggests that soot was once present but was either carried away or not preserved. *E*, The char/soot ratio is an indicator of the relative contribution of smoldering and flaming combustion. The ratio indicates that for this pond, the smoldering phase of the source wildfires dominated the flaming phase. Both types of combustion typically occur in nearly all fires, including impact fires, and the smoldering phase generally lasts longer.

Supplemental Tables

Table A1. Younger Dryas Boundary (YDB) Sites: Location, Age of YDB Layer, and Selected References

Sites (35)	Location	Continent	Modeled ages (cal BP)	Uncertainty (68% CI)	Latitude	Longitude	References
Well-dated YDB sites with biomass-burning proxies:							
Aalsterhut	Netherlands	Europe	12,780	35	~51.4272	5.5853	van Hoesel et al. 2012, 2014; Kinzie et al. 2014
Abu Hureyra	Syria	Asia	12,825	55	35.8667	38.4000	Bunch et al. 2012; Wittke et al. 2013; Kinzie et al. 2014
Arlington Canyon	California	North America	12,805	55	33.9886	−120.1580	Kennett et al. 2008, 2009*b*; Wittke et al. 2013; Kinzie et al. 2014
Blackville	South Carolina	North America	12,820	1080	33.3615	−81.3043	Bunch et al. 2012; Wittke et al. 2013; Kinzie et al. 2014
Blackwater Draw	New Mexico	North America	12,775	365	34.2756	−103.3261	Becker et al. 2009; LeCompte et al. 2012; Wittke et al. 2013; Wu et al. 2013; Andronikov et al. 2015
Bull Creek	Oklahoma	North America	12,840	75	~36.6400	−100.8500	Kennett et al. 2008, 2009*a*, 2009*b*; Bement et al. 2014; Kinzie et al. 2014
Daisy Cave	California	North America	12,730	320	34.0421	−120.3200	Erlandson et al. 1996; Erlandson 2007; Becker et al. 2009; Wittke et al. 2013; Kinzie et al. 2014
Indian Creek	Montana	North America	12,750	425	46.3144	−111.6302	Baker et al. 2008; Kinzie et al. 2014
Lake Cuitzeo	Mexico	South/Central America	12,850	570	19.9365	−101.1556	Israde-Alcántara et al. 2012; Wittke et al. 2013; Kinzie et al. 2014
Lake Hind	Canada	North America	12,745	180	49.4400	−100.6977	Firestone et al. 2007, 2010; Firestone 2009; Kennett et al. 2009*a*; Kinzie et al. 2014
Lindenmeier	Colorado	North America	12,775	180	40.9764	−105.1041	Kinzie et al. 2014
Lingen	Germany	Europe	12,735	85	52.5087	7.3138	Wittke et al. 2013; Kinzie et al. 2014
Lommel	Belgium	Europe	12,735	790	51.2362	5.2546	Beets et al. 2008; Tian et al. 2011; Wittke et al. 2013; Wu et al. 2013; Kinzie et al. 2014
Melrose	Pennsylvania	North America	12,255	2405	41.9254	−75.5104	Bunch et al. 2012; Wittke et al. 2013; Wu et al. 2013; Kinzie et al. 2014
Mucuñuque	Venezuela	South/Central America	12,845	630	8.7757	−70.8181	Mahaney et al. 2010*a*, 2010*b*, 2011*a*, 2011*b*; Mahaney and Krinsley 2012; Wittke et al. 2013
Murray Springs	Arizona	North America	12,750	235	31.5709	−110.1779	Firestone et al. 2007; Haynes 2007, 2008; Becker et al. 2009; Kennett et al. 2009*a*; Haynes et al. 2010; Andronikov et al. 2011; Pigati et al. 2012; Wittke et al. 2013; Wu et al. 2013; Kinzie et al. 2014
Ommen	Netherlands	Europe	12,750	560	52.5269	6.3635	Wittke et al. 2013; Kinzie et al. 2014

Table A1 (*Continued*)

Sites (35)	Location	Continent	Modeled ages (cal BP)	Uncertainty (68% CI)	Latitude	Longitude	References
Parangueo Lake	Mexico	South/Central America	12,843	228	20.3886	−101.2572	Domínguez-Vázquez 2012
Santa Maira	Spain	Europe	12,785	295	38.7302	−.2150	Kinzie et al. 2014
Sheriden Cave	Ohio	North America	12,840	120	40.9650	−83.4260	Tankersley 1997, 1999, 2009; Tankersley et al. 1997, 2001; Tankerseley and Landefeld 1998; Tankersley and Redmond 1999*a*, 1999*b*; Redmond and Tankersley 2005, 2011; Kinzie et al. 2014; Wittke et al. 2013; Wu et al. 2013
Stara Jimka	Czech Republic	Europe	12,805	70	49.0687	13.4029	Mentlík et al. 2010
Talega	California	North America	12,860	150	33.4702	−117.6004	Wittke et al. 2013
Topper	South Carolina	North America	12,785	185	33.0057	−81.4892	Goodyear 1999, 2005, 2006, 2010, 2013; Goodyear and Steffy 2003; Goodyear et al. 2007; Waters et al. 2009*a*, 2009*b*; LeCompte et al. 2012; Wittke et al. 2013; Kinzie et al. 2014
Inadequately dated YDB sites with biomass-burning proxies:							
Audenge	France	Europe	…	…	~44.7000	−1.0300	Ge et al. 2009
Caspian Sea	Asia	Asia	…	…	~38.6000	51.5000	Ge et al. 2009
Chobot	Canada	North America	…	…	52.9560	−114.7348	Firestone et al. 2007, 2010; Firestone 2009; Kennett et al. 2009*a*; Wittke et al. 2013; Kinzie et al. 2014
Gainey	Michigan	North America	…	…	42.8859	−83.6143	Wittke et al. 2013; Wu et al. 2013
Guil-Mt. Viso	France/Italy	Europe	…	…	44.6987	7.0346	Mahaney and Keiser 2012; Wittke et al. 2013; Mahaney et al. 2016*a*
Halls Cave	Texas	North America	…	…	30.1352	−99.5380	Kinzie et al. 2014
Kangerlussuaq	Greenland	Europe	…	…	67.1564	−50.0233	Kurbatov et al. 2010; Kinzie et al. 2014
Kimbel Bay	North Carolina	North America	…	…	34.9818	−78.7768	Wittke et al. 2013
Morley	Canada	North America	…	…	~51.14573	−114.8663	Firestone et al. 2007, 2010; Firestone 2009
Newtonville	New Jersey	North America	…	…	39.5695	−74.9108	LeCompte et al. 2012; Wittke et al. 2013; Wu et al. 2013; Kinzie et al. 2014
Paijan	Peru	South/Central America	…	…	ca. −7.7000	−79.3000	Ge et al. 2009
Paw Paw Cove	Maryland	North America	…	…	38.6974	−76.3422	LeCompte et al. 2012; Wittke et al. 2013
Watcombe Bottom	United Kingdom	Europe	…	…	50.5939	−1.2308	Wittke et al. 2013; Kinzie et al. 2014

Note. CI = confidence interval.

Table A2. Younger Dryas Boundary (YDB) Sites: Age of YDB Layer, with Types of YDB Proxies Present, as Discussed in Previous Publications

Sites (35)	Modeled ages (cal BP)	Uncertainty (68% CI)	AC/soot	Charcoal/ ash	Carbon spherules	Glass-like carbon	Fuller-enes	PAHs	Dark layer (black mat)	Platinum	Fe-, Si-rich spherules	High-temp. melt-glass	Nano-diamonds in sediments	Nano-diamonds, CS/GLC	Ir, Os, Ni, Co, Cr	Extinct mega-fauna	Human population decline
Dated carbon-rich YDB sites:																	
Aalsterhut	12,780	35		●	●	●			●					●			
Abu Hureyra	12,825	55	ND	●		●			●	●	●	●	●		●	●	
Arlington Canyon	12,805	55	●	●	●	●			●	●	●	●	●	●		●	
Blackville	12,820	1080	●	●	●	●				●	●	●		●	●		
Blackwater Draw	12,775	365	ND	●		●	●	●	●	●	●				●	●	●
Bull Creek	12,840	75	●							●			●				
Daisy Cave	12,730	320	ND	●		●	●	●	●		●						●
Indian Creek	12,750	425			●				●					●			●
Lake Cuitzeo	12,850	570		●	●				●	●	●		●			●	●
Lake Hind	12,745	180	ND	●	●	●			●	●			●		●	●	
Lindenmeier	12,775	180	●	●					●			●	●			●	
Lingen	12,735	85		●	●	●			●		●			●			
Lommel	12,735	790	ND	●	●	●			●	●	●			●			
Melrose	12,255	2405	●	●	●	●			●	●	●	●	●				
Mucuñuque	12,845	630			●				●		●	●	●				
Murray Springs	12,750	235	●	●	●	●	●	●	●	●	●	●	●		●	●	●
Ommen	12,750	560		●	●	●			●		●			●			
Parangueo Lake	12,843	228		●							●						
Santa Maira	12,785	295		●	●	●			●					●			
Sheriden Cave	12,840	120		●	●				●	●	●			●		●	●
Stara Jimka	12,805	70		●							●						
Talega	12,860	150							●		●						
Topper	12,785	185		●	●	●				●	●			●	●		●
Inadequately dated carbon-rich YDB sites:																	
Audenge	…	…		●	●	●			●		●	●		●			
Caspian Sea	…	…		●	●	●			●		●	●					
Chobot	…	…	ND	●	●	●			●	●	●	●	●	●			
Gainey	…	…	ND	●	●	●			●	●	●				●		●
Guil-Mt. Viso	…	…			●	●				●	●				●		
Halls Cave	…	…	●						●	●			●				
Kangerlussuaq	…	…			●						●		●				
Kimbel Bay	…	…			●						●						
Morley	…	…		●		●			●		●				●		
Newtonville	…	…		●					●	●	●		●				
Paijan	…	…		●	●	●			●		●	●		●			
Paw Paw Cove	…	…									●				●		●
Watcombe Bottom	…	…		●	●				●		●			●			
Total			7	27	24	21	3	3	27	17	29	11	13	14	10	8	9

Note. AC/soot = aciniform carbon; CS/GLC = carbon spherules/glass-like carbon; ND = not detected; PAHs = polycyclic aromatic hydrocarbons. Blank cell = not investigated.

Table A3. References for Younger Dryas Boundary (YDB) Biomass-Burning and Impact-Related Proxies or Consequences

Proxy	Proponents	Independent workers	Critics
Cosmic-impact spherules	Firestone et al. 2007, 2010; Firestone 2009; Bunch et al. 2012; Israde-Alcántara et al. 2012	Haynes et al. 2010; Mahaney et al. 2010*a*, 2010*b*, 2011*a*, 2011*b*, 2013; Redmond and Tankersley 2011; Fayek et al. 2012; LeCompte et al. 2012; Mahaney and Keiser 2012	Surovell et al. 2009; Pinter et al. 2011; Boslough et al. 2012; Pigati et al. 2012
Meltglass (scoria-like objects)	Bunch et al. 2012	Mahaney et al. 2010*a*, 2010*b*, 2011*a*, 2011*b*, 2013; Fayek et al. 2012; Mahaney and Krinsley 2012	...
Carbon spherules, glass-like carbon, aciniform carbon, PAHs, fullerenes	Firestone et al. 2007, 2010; Firestone 2009; Israde-Alcántara et al. 2012; Maiorana-Boutilier et al. 2016	Baker et al. 2008; Mahaney et al. 2010*a*, 2010*b*, 2011*a*, 2011*b*, 2013; Redmond and Tankersley 2011; Mahaney and Krinsley 2012	Scott et al. 2010; Pinter et al. 2011; Boslough et al. 2012; van Hoesel et al. 2012, 2014
Nanodiamonds	Firestone et al. 2007; Kennett et al. 2009*a*, 2009*b*; Kurbatov et al. 2010; Israde-Alcántara et al. 2012; Kinzie et al. 2014	Baker et al. 2008; Tian et al. 2011; Redmond and Tankersley 2011; Bement et al. 2014	Daulton et al. 2010; Pinter et al. 2011; Boslough et al. 2012; van Hoesel et al. 2012, 2014
Iridium	Firestone et al. 2007, 2010; Firestone 2009	Haynes et al. 2010; Andronikov et al. 2011, 2016*a*; Marshall et al. 2011	Paquay et al. 2009; Pinter et al. 2011; Boslough et al. 2012; Pigati et al. 2012
Platinum	Mahaney et al. 2016*b*; Moore et al. 2017	Petaev et al. 2013*a*	...
Osmium	...	Beets et al. 2008; Sharma et al. 2009; Andronikov et al. 2011; Wu et al. 2013	Paquay et al. 2009
Nickel, cobalt, chromium, thorium, ^{14}C, ^{10}Be, ^{26}Al, REEs	Firestone et al. 2007, 2010; Firestone 2009	Melott et al. 2010; Andronikov et al. 2011	...
Extinctions, human population declines	Firestone et al. 2007, 2010; Firestone 2009; Anderson et al. 2011	Melott et al. 2010; Andronikov et al. 2011	...

Note. PAHs = polycyclic aromatic hydrocarbons; REEs = rare earth elements.

Table A4. Quantification of Younger Dryas Boundary (YDB) Biomass-Burning Proxies

	Sites		Size			YDB proxies			Background		
YDB carbon proxies	Total	Tested	Maximum	Minimum	Proxy units	Average	Maximum	Minimum	Average	Maximum	Minimum
Charcoal	31	31	~6 cm	125 μm	μm g/kg	3.9	27.9	.01	.1	1.5	0
Carbon spherules	24	24	2.5 mm	1 μm	*n*/kg	490	3690	192	13	160	0
Glass-like carbon	20	20	~6 cm	~250 μm	μm g/kg	.45	16	.03	~0	.02	0
Aciniform carbon (soot)	7	15	~150 nm	10 nm	ppm	1234	6100	21	0	0	0
Fullerenes	3	3	~1 nm	~.5 nm	...[a]	...[a]	...[a]	...[a]	0	0	0
PAHs	3	3	~1 μm	~.5 μm	...[a]	...[a]	...[a]	...[a]	0	0	0

Note. PAHs = polycyclic aromatic hydrocarbons.
[a] Detected, not quantified.

Table A5. Aciniform carbon at 16 Younger Dryas Boundary Sites: Location, Sample Number, and Concentrations with Uncertainties

Site, sample no.	AC/soot (ppm)	Error (ppm)
Abu Hureyra, Syria:		
ES15	0	0
Arlington Canyon, California:		
AC344	13	1
AC343	2460	250
ARL-4B	0	0
AC342	0	0
ARL-3B	0	0
AC341	0	0
ARL-2B	0	0
AC340	0	0
ARL-1B	0	0
Blackville, South Carolina:		
T13–0-BU	2000	200
T13–60-BU (LB1)	0	0
T13–120-BU	0	0
Blackwater Draw, New Mexico:		
BW-F-BU	0	0
BW-DT-BU (duplicate)	0	0
BW-D-BT-BU (duplicate)	0	0
BW-D-B-BU	0	0
BW-DM-BU	0	0
BW-D/C-BU	0	0
BW-BSW-BU	0	0
BW-C-M-BU	0	0
BW-AE-BU	0	0
BW-CLW-BU (Clovis)	0	0
BW-FOW-BU (Folsom)	0	0
BW-LK-B-BU (Lake)	0	0
BW-LK-T-BU (Lake)	0	0
Bull Creek, Oklahoma:		
BL247	0	0
BL151	11	50
BL152	500	40
BL153	400	0
Daisy Cave, California:		
Extracted residue (3a)	0	0
Untreated residue (3b)	0	0
Gainey, Michigan:		
G-CL	0	0
Lake Cuitzeo, Mexico:		
270	0	0
275	0–2600[a]	560
280	0	0
290	0	0
Lake Hind, Manitoba, Canada:		
H-2-BU	0	0
H-26/30-BU	0	0
H-32-BU	0	0
Hall's Cave, Texas:		
HC 349	0	0
HC 351	0	0
HC 352	0	0
HC 354	0	0
HC 356	0	0
HC 358	0	0
HC 362	0	0
HC 363	0	0
HC 364	2400	200
HC 365	400	40
HC 367	0	0
HC 369	0	0
HC 372	0	0
Lehner site, Arizona:		
LEHN-MT	0	0
LEHN-MB	0	0
LEHN-M/CL	0	0
Lommel, Belgium:		
HK3	0	0
SOE-3	0	0
LM219	0	0
LM220	0	0
LM221	0	0
Melrose, Pennsylvania:		
Y2–6	100	10
Y2–9	5	1
Y2–11	20	2
Murray Springs, Arizona:		
MS-3B-T-BU	0	0
MS-3B-B-BU	0	0
MSA-17 (HAN)	20	5
MU181	200	20
MU177	6100	610
MU178	0	0
MS-42-BU	0	0
MS-N-3-CL	0	0
MS-N-2-M	0	0
MS-F-BU	0	0
MS-H-BU	0	0
Newtonville, New Jersey (UP):		
COA-1	200	20
COB-1	0	0
Sheriden Cave, Ohio:		
Top +5 to +40	0[b]	0
Block-mid	4000[b]	200
Bottom −10 to −15	0[b]	0

Note. AC/soot = aciniform carbon.

[a] 0 in this study; 2600 in Maiorana-Boutilier et al. (2016).

[b] From Maiorana-Boutilier et al. (2016).

Table A6. Concentrations for Pt, AC/Soot, Charcoal, Nanodiamonds, and Magnetic Spherules in 10 Key Sites Shown in Figure 9

Site, depth (cm)	Platinum (ppb)	Soot (ppm)	Charcoal (g/kg)	Nanodiamonds (ppb)	Mag sph (no./kg)
Arlington Canyon, California:					
97.0	<.1		115	0	
117.5			2	0	
123.5			0	0	
146.5	<.1		0	0	
167.5			0	0	
181.0			18	0	
196.5	<.1		413	0	0
216.0			131	0	
227.5	.6		31	0	
239.5	.2		2	0	0
246.5			22	0	
268.5			76	0	
298.5	<.1		65	0	0
341.5	.3		5	0	
384.5			13	18	
394.0	.1		261	1342	0
404.5			430	363	0
414.5	<.1		0	0	
461.5	<.1				0
466.5					0
472.0					12
477.5	.1				44
482.5		13	51	35	0
488.0	<.1	2460	58	26	0
489.0		0	132	0	
492.0	<.1	0	102	0	0
493.0		0	148	54	0
495.5	1.0	0	849	15	0
497.0	.5	0	435	45	0
500.5	.4	0	258	493	24
501.0	1.1	0	268	865	58
Blackville, South Carolina:					
7.5				0	
106.7				0	190
121.9				0	115
137.2				0	90
152.4				0	67
167.6	.1			3	206
182.9	.5	2000		313	525
198.1	<.1	0		0	0
213.4		0		0	0
228.6				0	2
243.8				0	0
259.1				0	5
Blackwater Draw, New Mexico:					
1237.75	<.1	0	0		174
1237.90	<.1		0		0
1238.06	<.1		0		0
1238.14			0		
1238.17		0	0		0
1238.31					0
1238.32	.3	0	0		770
1238.37	1.2, .2	0	0		768
1238.38		0			
1238.40	<.1	0	0		317
1238.46		0	0		0
1238.65	<.1		0		0

Table A6 (*Continued*)

Site, depth (cm)	Platinum (ppb)	Soot (ppm)	Charcoal (g/kg)	Nanodiamonds (ppb)	Mag sph (no./kg)
1238.75	<.1	0	0		0
1239.60	.6		0		0
Bull Creek, Oklahoma:					
209.3	.6	0		0	
230.0	.5			0	
289.0	.5			0	
298.0	.5			0	
307.0	.7	11		102	
328.0	.8	500		23	
351.0	.6	400		15	
362.0				0	
386.0				0	
Hall's Cave, Texas:					
349.0		0		4	
351.0		0		1	
352.0		0		1	
353.0				11	
354.0		0		15	
355.0				0	
356.0		0		23	
357.0				23	
358.0		0		7	
359.0				4	
360.0				23	
361.0	.6			12	
362.0	.4	0		1	
363.0	.5, .4	0		26	
364.0	.4	2400		105	
365.0	.4, .3	400		61	
366.0	.4			0	
367.0	.4	0		0	
368.0				0	
369.0		0		0	
370.0				0	
372.0		0		1	
Lake Cuitzeo, Mexico:					
220			429	3	114
225			0		96
230			0		
235			288	6	120
240			793		
245			1749		
250			2831		
255			8028		126
260			2992		
265			76,952	10	79
270		0	23,997	1	311
275		0–7100[a]	22,818	45	214
280		0	14,886	493	2054
290		0	8602	1	216
300			10,689	29	0
310			28,856	1	0
320			12,780	0	0
330			6907		0
340			1196	3	0
350			988		0
360				0	0
Melrose, Pennsylvania:					
10.0	.1				310
19.0	<.1	100		0	3110

Table A6 (*Continued*)

Site, depth (cm)	Platinum (ppb)	Soot (ppm)	Charcoal (g/kg)	Nanodiamonds (ppb)	Mag sph (no./kg)
25.0	3.8	5		66	1190
33.0	8.1	20		16	71
43.0	.7			0	210
Murray Springs, Arizona:					
16.0	<.1		.0		0
21.0			.0		0
26.0	<.1		.0	0	0
31.0			.0	0	0
36.0	<.1		.0	0	0
41.5	<.1	0			0
44.0		0			
44.5		0			
44.8	.4	20, 200	.0	0	8
45.5		0			
46.5	4.4	6100, 0, 0	.1	426	55, 109
48.3	.1	0	.0	0	9
52.0	.1		.0	0	0
52.5		0			
57.0	.7, .7		.0	0	0
63.0	<.1		.0	0	0
Newtonville, New Jersey:					
35.0					0
40.0		200		64	1840
45.0		0		0	243
Sheriden Cave, Ohio:					
17.5	.2	0[b]	.3	0	0
37.5	<.1		.1	0	0
42.3	.9		.2	0	40
43.8		4000[b]			
45.3	.9		.7	108	108
48.5	.1		.5	0	0
53.5	<.1		.7	0	0
58.5	<.1	0[b]	.5	0	0
66.0	<.1		.5	0	0
76.0	<.1		.3	0	0

Note. Of the 10 sites, seven contain aciniform carbon/soot and two others contain black carbon/soot. Mag sph = magnetic spherules.
[a] 0 from this study; 7100 from Maiorana-Boutilier et al. (2016).
[b] From Maiorana-Boutilier et al. (2016)

Table A7. Calibration Differences among Five Radiocarbon Curves for Younger Dryas Boundary ^{14}C Date of 10,900 ± 100 ^{14}C y BP

^{14}C curve	Calibrated age	Δ vs. IntCal13 (y)
IntCal13	12,819	0
Fairbanks	12,840	21
IntCal93	12,874	55
IntCal04	12,891	72
IntCal98	12,936	117

Note. The ^{14}C date of 10,900 ± 100 ^{14}C y BP is from Firestone et al. (2007).

Table A8. Comparison of Calibration Curves Used by Marlon et al. (2009)

			Difference				
Lake	^{14}C Date[a]	GCD[a]	IntCal93	IntCal98	IntCal04	IntCal13	Maximum Δ
Mumbo Lake	12,210 ± 100	14,658	−398	−135	−533	−503	−533
Burnt Knob Lake	11,922 ± 83	14,050	−190	55	−262	−293	−293
Pintlar Lake	10,690 ± 100	12,883	−213	−177	−192	−268	−268
Foy Lake	9820 ± 95	11,250	−206	−7	11	11	−206
Dead Horse Lake	11,910 ± 120	13,949	−99	131	−181	−193	−193
Baker Lake	11,100 ± 130	13,132	−102	−22	−101	−177	−177
Ruppert Lake	10,740 ± 80	12,820	−90	−36	−54	−157	−157
Enos Lake	11,620 ± 50	13,604	−34	51	−133	−153	−153
Hertel Lake	10,510 ± 60	12,585	−103	−76	−82	−135	−135
East Sooke Fen	11,700 ± 140	13,669	−49	98	−112	−127	−127
Whyac Lake	10,860 ± 130	12,915	−95	−22	−62	−122	−122
Bolan Lake	11,010 ± 65	13,002	−82	12	−48	−121	−121
Pixie Lake	11,750 ± 100	13,705	−15	103	−108	−118	−118
Moon Lake	11,770 ± 80	13,720	0	107	−104	−117	−117
Siesta Lake	11,280 ± 60	13,207	3	72	−38	−61	72
Boomerang Lake	10,270 ± 60	12,070	82	15	−27	−30	82
Sharkey Lake	10,255 ± 45	12,040	84	10	−38	−44	84
Bluff Lake	11,550 ± 90	13,471	9	102	−61	−89	102
Xindi Lake	10,180 ± 120	11,844	123	23	−1	−5	123
Lac J'Arrive	10,040 ± 100	11,579	128	28	15	12	128
Como Lake	10,260 ± 230	12,003	130	21	5	−34	130
Lac Albion	11,140 ± 120	12,993	107	153	61	−8	153
Lake Tulane	10,960 ± 50	12,827	53	154	80	−3	154
Cygnet Lake	11,800 ± 190	13,755	−45	172	−95	−88	172
Slough Creek	11,800 ± 190	13,755	−45	172	−95	−88	172
Crane Lake	11,200 ± 480	13,098	12	182	46	32	182
Battle Ground Lake	10,490 ± 360	12,260	199	−2	−24	−62	199
Porphyry Lake	12,540 ± 200	14,630	−20	199	17	114	199
Lost Lake	12,460 ± 50	14,482	18	256	52	129	256
Chihuahuenos Bog	11,850 ± 80	13,711	89	276	−8	−44	276
Swamp Lake	13,690 ± 340	16,284	36	133	44	292	292
Little Lake	11,913 ± 60	13,790	148	305	−11	−61	305
Hunter's Lake	11,970 ± 89	13,827	73	347	12	1	347
Walker Lake	12,240 ± 120	14,160	130	396	54	89	396
East Lake	13,400 ± 60	15,601	219	445	324	520	520

Note. Radiocarbon dates, uncertainties, and calibrated ages from the Global Charcoal Database (GCD 2013). Each lake-core date is the one closest to the Younger Dryas boundary age of 12,900 ± 100, as used in Marlon et al. (2009). Next are differences between the published calibrated GCD date and the results of calibrating the identical radiocarbon date with other calibration curves: IntCal93, IntCal98, IntCal04, and IntCal13 (Stuiver and Reimer 1993; Stuiver et al. 1998; Reimer et al. 2004, 2013). In the Marlon et al. study, all curves were used except the latest curve, IntCal13, which is shown here to highlight the difficulties of using different calibration curves. Maximum differences for the identical date are +520 and −533 cal BP (last column). Hence, dated layers in 35 lake cores could appear to differ in age by as much as 533 y, even though coeval. This also refutes the claim of ±50-y precision by Marlon et al. (2009).

[a] Dates are from GCD (2013).

Table A9. Age Uncertainties for 35 Selected North American Lake-Core Records

	From GCD		With IntCal13 calibration curve	
Lake	^{14}C date	Error (68% CI)	Cal BP date	Error (68% CI)
Siesta Lake	11,280	60	13,146	57
Enos Lake	11,620	50	13,451	58
Ruppert Lake	10,740	80	12,663	58
Lake Tulane	10,960	50	12,824	70
Bolan Lake	11,010	65	12,881	82
Bluff Lake	11,550	90	13,382	87
Moon Lake	11,770	80	13,603	87
Chihuahuenos Bog	11,850	80	13,667	92

Table A9 (*Continued*)

	From GCD		With IntCal13 calibration curve	
Lake	^{14}C date	Error (68% CI)	Cal BP date	Error (68% CI)
Pintlar Lake	10,690	100	12,615	93
Little Lake	11,913	60	13,729	95
East Lake	13,400	60	16,121	103
Pixie Lake	11,750	100	13,587	104
Sharkey Lake	10,255	45	11,996	106
Hertel Lake	10,510	60	12,450	114
Burnt Knob Lake	11,922	83	13,757	120
Whyac Lake	10,860	130	12,793	121
Baker Lake	11,100	130	12,955	123
Hunter's Lake	11,970	89	13,828	123
Lac Albion	11,140	120	12,985	123
Boomerang Lake	10,270	60	12,040	145
East Sooke Fen	11,700	140	13,542	147
Dead Horse Lake	11,910	120	13,756	149
Foy Lake	9820	95	11,261	164
Crane Lake	11,200	480	13,130	179
Lost Lake	12,460	50	14,611	194
Lac J'Arrive	10,040	100	11,591	196
Mumbo Lake	12,210	100	14,155	207
Cygnet Lake	11,800	190	13,667	218
Slough Creek	11,800	190	13,667	218
Xindi Lake	10,180	120	11,839	254
Walker Lake	12,240	120	14,249	257
Porphyry Lake	12,540	200	14,744	366
Como Lake	10,260	230	11,969	369
Battle Ground Lake	10,490	360	12,198	477
Swamp Lake	13,690	340	16,576	486
Average uncertainty				179

Note. Lake names, ^{14}C dates, and age uncertainties at 68% confidence interval (CI) from the Global Charcoal Database (GCD 2013), followed by calibrated ages and uncertainties using the IntCal13 calibrations curve. These dates were chosen because each is closest in age to the YDB age (12,900 cal BP), the age used in Marlon et al. (2009). For these 35 North American lake records, the average age uncertainty of ±179 y is significantly higher than the precision of ±50 y claimed by Marlon et al. (2009).

Table A10. Lake Cores (129)

Site name	GCD ID	No. PTS	Continent	Country	State/province	Latitude	Longitude	Elevation (m)	Source
17940 core	95	17	Asia	(Ocean)		20.1167	117.3833	−1727	GCD 2013
Ackgol	1125	50	Asia	Turkey		37.3000	33.4400	1000	GCD 2013
Aligol	468	7	Asia	Georgia		41.6333	44.0167	1550	GCD 2013
Appleman Lake	None	144	North America	USA	Indiana	41.6230	−85.2130	295	Lininger 2007
Aracatuba	1095	8	South America	Brazil		−25.9167	−48.9833	1500	GCD 2013
Baker	4	99	North America	USA	Idaho	45.8919	−114.2619	2300	GCD 2013
Battle Ground Lake	256	283	North America	USA	Washington	45.8000	−122.4917	154	GCD 2013
Bear Lake	None	15	North America	USA	Arizona	36.3710	−112.1470	2779	Weng and Jackson 1999
Big Fish	None	117	North America	USA	Michigan	42.8860	−83.3910	322	Ballard and Lowell 2009
Binnewater	1099	12	North America	USA	New York	41.4100	−74.5519	256	Robinson et al. 2005
Bluff	9	90	North America	USA	California	41.3467	−122.5575	1921	GCD 2013
Bolan	8	149	North America	USA	Oregon	42.0200	−123.4600	1637	GCD 2013
Boomerang Lake	363	17	North America	USA	British Columbia	49.1800	−124.1500	360	GCD 2013
Browns Pond–BR92	None	71	North America	USA	Virginia	38.1550	−79.6160	621	Kneller and Peteet 1999
Burnt Knob	3	86	North America	USA	Idaho	45.7044	−114.9867	2250	GCD 2013

Table A10 (*Continued*)

Site name	GCD ID	No. PTS	Continent	Country	State/province	Latitude	Longitude	Elevation (m)	Source
Cambara do Sul	90	6	South America	Brazil		−29.0525	−50.1011	1040	GCD 2013
Campbell Lake	None	62	North America	USA	California	41.5330	−123.1070	1757	Briles 2008
Canal de la Puntilla	554	18	South America	Chile		−40.9500	−72.9000	120	GCD 2013
Cheremushuka bog	684	16	Asia	Russia		52.7500	108.0833	462	GCD 2013
Chihuahueros Bog	116	176	North America	USA	New Mexico	36.0472	−106.5083	2925	GCD 2013
Coast Trail Pond	132	150	North America	USA	California	37.9853	−122.8000	230	Anderson 2005
Como	21	10	North America	USA	Colorado	37.5500	−105.5000	3523	GCD 2013
Crane	22	8	North America	USA	Arizona	36.7167	−112.2167	2590	GCD 2013
Cygnet	1	198	North America	USA	Wyoming	44.6628	−110.6161	2530	GCD 2013
Dead Horse Lake	129	49	North America	USA	California	42.5606	−120.7781	2248	GCD 2013
Dongganchi site	97	59	Asia	China		40.2000	116.0000	49	GCD 2013
Duguldzeiri River bog	685	8	Asia	Russia		54.4500	109.5333	529	GCD 2013
Duliha bog	683	10	Asia	Russia		51.5167	105.0000	510	GCD 2013
Dyanushka	456	30	Asia	Russia		65.0300	125.0300	33	GCD 2013
East Lake	474	69	North America	USA	California	37.1779	−119.0277	2863	GCD 2013
East Sooke Fen	198	58	North America	Canada	British Columbia	48.3519	−123.6817	155	GCD 2013
El Salto	143	123	South America	Chile		−41.6400	−73.0961	67	GCD 2013
Enos	24	24	North America	Canada	British Columbia	49.2800	−124.1500	50	GCD 2013
Ertangcun	618	22	Asia	Mongolia		35.0100	107.6500	1050	GCD 2013
Eski Acigol	772	103	Asia	Turkey		38.5500	34.5400	1270	GCD 2013
Fish	391	13	North America	USA	Minnesota	43.8500	−95.0440	423	GCD 2013
Foy	7	417	North America	USA	Montana	48.1658	−114.3592	1006	GCD 2013
Fracas Lake	None	20	North America	USA	Arizona	36.6310	−112.2390	2524	Weng and Jackson 1999
Graham lake	1092	68	North America	Canada	Ontario	45.1833	−77.3500	381	Fuller 1997
Griblje Marsh	None	107	Europe	Slovenia		45.5675	15.2819	160	Andric 2011
Head Lake	None	13	North America	USA	Colorado	37.6939	−105.7338	2294	Jodry et al. 1989
High lake	1093	31	North America	Canada	Ontario	44.5167	−76.6000	192	GCD 2013
Hunter's Lake	134	109	North America	USA	Colorado	37.6083	−106.8444	3516	GCD 2013
Jan	217	90	North America	USA	Alaska	66.0300	−147.5533	223	GCD 2013
Kettle	None	17	North America	USA	North Dakota	48.6100	−103.6200	610	GCD 2013
La Yeguada	357	263	South America	Panama		8.4500	−80.8500	650	GCD 2013
Lac Albion	205	22	North America	Canada	Quebec	45.6708	−71.3250	320	GCD 2013
Lac aux Atocas	400	10	North America	Canada	New Brunswick	45.5372	−73.3108	114	Carcaillet and Richard 2000
Lac du Lait	631	6	Europe	France		45.3164	6.8136	2180	GCD 2013
Lac Hertel	312	45	North America	Canada	Quebec	45.6833	−74.0500	75	GCD 2013
Lac J'Arrive	209	18	North America	Canada	Quebec	49.2472	−65.3764	56	GCD 2013
Lac Ouellet	411	10	North America	Canada	Quebec	47.5327	−68.9439	300	Flannigan et al. 2001
Lagaccione	845	17	Europe	Italy		42.5667	11.8500	355	GCD 2013
Lago Condorito	144	78	South America	Chile		−41.7500	−73.1167	60	GCD 2013
Lago del Greppo	490	38	Europe	Italy		44.1167	11.6667	1442	GCD 2013
Lago di Gembro	634	44	Europe	Italy		46.1644	10.1544	1350	GCD 2013
Lago di Origlio	258	45	Europe	Switzerland		46.0512	8.9424	416	GCD 2013
Lago di Pergusa	714	13	Europe	Italy		37.5167	14.3000	674	GCD 2013
Lago Piccolo di Avigliana	381	79	Europe	Italy		45.0500	7.3833	356	GCD 2013
Lago Pollux	150	172	South America	Argentina		−45.6756	−71.8629	640	GCD 2013
Lagoa do Caco	119	23	South America	Brazil		−2.9702	−43.2678	120	GCD 2013
Laguna Chorreras	61	18	South America	Ecuador		−2.7500	−79.1667	3700	GCD 2013
Laguna de Chochos	63	22	South America	Peru		−7.6363	−77.4746	3285	GCD 2013
Laguna Lincoln	1069	25	South America	Chile		−45.3667	−74.0667	19	GCD 2013
Laguna Pallcacocha	62	25	South America	Ecuador		−2.7500	−79.1667	4060	GCD 2013
Laguna Six Minutes	1071	17	South America	Chile		−46.4167	−74.3333	15	GCD 2013
Lake Bled	None	25	Europe	Slovenia		46.3667	14.1000	475	Andric 2011

Table A10 (*Continued*)

Site name	GCD ID	No. PTS	Continent	Country	State/province	Latitude	Longitude	Elevation (m)	Source
Lake Cuitzeo	None	15	South America	Mexico	Michoacán	19.9360	−101.1550	1833	Israde-Alcántara et al. 2012
Lake Hind	None	16	North America	Canada	Manitoba	49.4390	−100.0010	434	Boyd et al. 2003
Lake Hordorli	733	8	Asia	Indonesia		−2.5330	140.5500	680	GCD 2013
Lake Santa Rosa	562	13	South America	Bolivia		−14.4769	−67.8747	350	GCD 2013
Lake Sixteen	None	107	North America	USA	Michigan	42.7560	−83.2860	301	Ballard and Lowell 2009
Lake Titicaca	58	40	South America	Bolivia		−16.1344	−69.1553	3810	GCD 2013
Lake Tulane	557	6	North America	USA	Florida	27.5862	−81.5033	35	GCD 2013
Lake Van	73	38	Asia	Turkey		38.5578	42.5386	1648	GCD 2013
Lepue	147	242	South America	Chile		−42.8000	−73.7000	152	GCD 2013
Lily Pond	None	183	North America	USA	California	39.3150	−122.7100	1241	Beaty and Taylor 2008
Little Lake	769	193	North America	USA	Oregon	44.1680	−123.5835	703	GCD 2013
Lobsigensee	261	31	Europe	Switzerland		47.0306	7.2982	514	GCD 2013
Loch a'Phuinnd	758	13	Europe	UK		57.3667	−7.2667	10	GCD 2013
Loch Buailaval Beag	757	21	Europe	UK		58.2667	−6.7667	50	GCD 2013
Lost Lake	999	26	North America	USA	Alaska	45.8242	−123.5792	449	GCD 2013
MD95-2042	542	19	Europe	(Ocean)		37.7500	−10.1667	−3146	GCD 2013
MD97-1240	1105	136	Asia	(Ocean)		2.0333	141.7667	−2547	Thevenon et al. 2004
Mizorogaike	672	6	Asia	Japan		35.0586	135.7694	75	GCD 2013
Montezuma Well	31	15	North America	USA	Arizona	34.0000	−112.0000	1125	Davis and Shafer 1992
Moon	394	15	North America	USA	North Dakota	46.8500	−98.1500	456	GCD 2013
Mumbo	12	56	North America	USA	California	41.1913	−122.5092	1860	GCD 2013
Navarres	637	20	Europe	Spain		39.1000	−.6833	225	GCD 2013
Pamerkiai	None	27	Europe	Lithuania		54.3125	24.7311	150	Stančikaitė et al. 2009
Parangueo crater lake	None	71	South America	Mexico	Guanajuato	20.4320	−101.2510	1688	Domínguez-Vázquez 2012
Pintlar	6	169	North America	USA	Montana	45.8406	−113.4403	1921	GCD 2013
Pixie	199	41	North America	Canada	British Columbia	48.5964	−124.1967	70	GCD 2013
Plan Bouchet	640	17	Europe	France		45.2469	6.5661	2405	GCD 2013
Porphyry	201	15	North America	Canada	British Columbia	48.9056	−123.8333	1100	GCD 2013
Potts Mountain Lake	None	10	North America	USA	Virginia	37.6010	−80.1390	1094	Watts 1979
Puerto del Hambre	162	19	South America	Chile		−53.6000	−70.9167	3	GCD 2013
Puerto Haberton	170	23	South America	Chile		−54.8833	−67.1667	20	GCD 2013
Punta Arenas	160	21	South America	Chile		−53.1500	−70.9500	75	GCD 2013
Quilichao-1	77	25	South America	Colombia		3.1000	−76.5167	1020	GCD 2013
Reservoir-2	None	563	North America	USA	Montana	45.1300	−113.4600	2161	Gage 2008
Rio Rubens	158	247	South America	Argentina		−52.1375	−71.8814	220	GCD 2013
Ruppert	220	354	North America	USA	Alaska	67.0711	−154.2458	230	GCD 2013
Sanger Lake	None	83	North America	USA	California	41.9020	−123.6470	1557	Briles 2008
São Francisco de Assis	118	13	South America	Brazil		−29.5867	−55.2172	100	GCD 2013
Serra Campos Gerais	84	12	South America	Brazil		−24.6667	−50.2167	1200	GCD 2013
Sharkey	263	8	North America	USA	Minnesota	44.5942	−93.4136	305	GCD 2013
Siesta Lake	179	120	North America	USA	California	37.8500	−119.6667	2430	GCD 2013
Siles Lake	301	10	Europe	Spain		38.4000	−2.5000	1320	GCD 2013
Sithylemenkat Lake	None	7	North America	USA	Alaska	66.1261	−151.3889	219	Earle et al. 1996
Slack Lake	None	88	North America	USA	Michigan	42.8720	−83.6100	282	Ballard and Lowell 2009
Slough Creek Pond	2	192	North America	USA	Wyoming	44.9183	−110.3467	1884	GCD 2013
Sonenuma Bog	452	11	Asia	Japan		35.2358	136.1961	86	GCD 2013

Table A10 (*Continued*)

Site name	GCD ID	No. PTS	Continent	Country	State/province	Latitude	Longitude	Elevation (m)	Source
Soppensee	260	59	Europe	Switzerland		47.0802	8.0833	596	GCD 2013
Stara Jimka	None	45	Europe	Czech Republic		49.0682	13.4017	1160	Mentlík et al. 2010
Surucucho	60	45	South America	Ecuador		−3.0625	−78.0000	3180	GCD 2013
Swamp Lake	40	11	North America	USA	California	37.9500	−119.8167	1554	GCD 2013
Swift Lake	None	38	North America	USA	Michigan	42.0760	−85.8850	269	Ballard and Lowell 2009
Szabo Pond	None	7	North America	USA	New Jersey	40.4000	−74.4830	29	Watts 1979
Taylor Lake	1147	80	North America	USA	California	41.3614	−122.9675	1979	Briles 2008
Tompuda bog	686	17	Asia	Russia		55.1333	109.7667	459	GCD 2013
Torres del Paine 2	154	21	South America	Chile		−51.0833	−73.0667	100	GCD 2013
Trebol Lake	92	82	South America	Argentina		−41.0713	−71.4916	758	GCD 2013
Tumalo Lake	1130	392	North America	USA	Oregon	44.0218	−121.5438	1536	GCD 2013
Walker	202	10	North America	Canada	British Columbia	48.5292	−124.0022	950	GCD 2013
Whyac	200	14	North America	Canada	British Columbia	48.6722	−124.8444	15	GCD 2013
Wien Lake	None	17	North America	USA	Alaska	64.3610	−151.2980	305	Tinner and Hu 2003
Xindi	221	238	North America	USA	Alaska	67.1117	−152.4917	240	GCD 2013
Xujianan	617	23	Asia	Mongolia		35.5000	106.0000	1620	GCD 2013

Note. Global Charcoal Database (GCD 2013) identification number (GCD ID), name, number of samples with interpolated dates (No. PTS), continent, state/province, latitude and longitude, elevation in meters, and data source. These sites were selected because each contained one or more sedimentary samples dating between 13,400 and 12,300 cal BP, and the data included radiocarbon dates, depths, and charcoal values, recorded as concentration or influx.

Table A11. Bayesian Synchroneity of Climate, Biomass Burning, and Impact-Related Proxies at Younger Dryas (YD) Onset

		Biomass-burning synchroneity sequence												
		Unmodeled (BP)					Modeled (BP): A_{model} = 227, $A_{overall}$ = 227							
			68.2% CI		95.4% CI		68.2% CI		95.4% CI					
Groups	Sites	Cal BP	From	To	From	To	From	To	From	To	Mean	σ	*A*	*C*
L difference							−1	100	−1	241	84	78		95.6
End boundary							12,812	12,748	12,837	12,686	12,769	40		98.1
Platinum peak, GISP2 ice core	1	12,840 ± 258	13,099	12,583	13,356	12,326	12,841	12,773	12,908	12,727	12,812	43	138.7	99.8
YD cooling onset:														
GISP2 ice core	1	12,840 ± 258	13,099	12,583	13,356	12,326	12,841	12,773	12,908	12,727	12,812	43	138.7	99.8
NGRIP ice core	1	12,846 ± 138	12,985	12,709	13,123	12,571	12,840	12,774	12,904	12,733	12,812	41	132.0	99.8
GRIP ice core	1	12,840 ± 138	12,979	12,703	13,117	12,565	12,840	12,774	12,903	12,733	12,812	40	133.2	99.8
YDB charcoal, Santa Barbara Basin	1	12,970 ± 205	13,177	12,765	13,380	12,561	12,841	12,774	12,914	12,732	12,815	44	104.7	99.8
YD onset, lake charcoal:														
North America	65	12,905 ± 350	13,256	12,556	13,604	12,208	12,840	12,773	12,910	12,728	12,812	44	135.5	99.7
South America	28	12,850 ± 235	13,086	12,615	13,320	12,381	12,840	12,773	12,908	12,729	12,812	43	137.4	99.8
Europe	19	12,835 ± 220	13,056	12,616	13,275	12,396	12,840	12,774	12,907	12,728	12,812	42	138.1	99.8
Asia	17	12,950 ± 225	13,176	12,725	13,400	12,501	12,841	12,774	12,913	12,731	12,814	43	116.1	99.8
YDB impact proxies, land:														
North America	13	12,779 ± 29	12,810	12,750	12,838	12,722	12,822	12,775	12,844	12,749	12,797	24	97.1	99.8
South America	3	12,813 ± 36	12,850	12,777	12,886	12,742	12,834	12,783	12,863	12,757	12,809	26	114.4	99.9
Europe	6	12,845 ± 201	13,048	12,644	13,247	12,444	12,840	12,774	12,907	12,729	12,812	42	136.6	99.8
Asia	1	12,825 ± 55	12,882	12,770	12,936	12,716	12,838	12,779	12,881	12,750	12,812	32	119.9	99.8
Start boundary							12,877	12,794	12,976	12,770	12,854	56		98.1

Note. The Bayesian modeled ages for 13 sites or groups are separated by a minimum of 0 y (statistically calculated as −1) at the 68% and 95% confidence intervals (CIs; "L difference"). The mean age is 12,854 ± 56 (12,910–12,798) cal BP ("Start boundary"), which overlaps the published YDB age in Kennett et al. (2015) and Bunch et al. (2012). A_{model} and $A_{overall}$ represent OxCal's calculated agreement index, which is expected to be ≥60, as is the case. *C* represents the convergence integral and should usually be >95%, as is the case. GISP2 = Greenland Ice Sheet Project 2; NGRIP = North Greenland Ice Core Project; GRIP = Greenland Ice Core Project; YDB = YD boundary.

Table A12. Estimated Comparison of AC/Soot Concentrations at the Younger Dryas Boundary (YDB) versus the Cretaceous-Tertiary (K-Pg) Boundary

	Younger Dryas boundary				K-Pg boundary			
	Straight average		Weighted average		Straight average		Weighted average	
	Value	Error	Value	Error	Value	Error	Value	Error
Footprint concentration:								
AC/soot (g/cm^2)	.0117	.0133	.0146	.0047	.0035	.0068	.0044	.0018
Percent biomass burned:								
Contemporary biomass	5.865	6.637	7.279	2.345	1.762	3.411	2.196	.882
Precivilization biomass	2.346	2.655	2.912	.938	.705	1.365	.879	.353
Area biomass burned:								
Contemporary biomass (km^2)	6.228E+06	7.049E+06	7.730E+06	2.491E+06	1.871E+06	3.623E+06	2.333E+06	9.371E+05
Percent land area burned:								
Earth	4.180	4.731	5.188	1.672	1.256	2.431	1.566	.629
Northern Hemisphere	6.228	7.049	7.730	2.491	1.871	3.623	2.333	.937
YDB vs. modern burn rate:								
YDB/modern	1.934	2.189	2.401	.773	.581	1.125	.724	.291

Note. Various calculations for 7 YDB sites versus 11 K-Pg sites. Data are from Wolbach et al. (1990). AC/soot = aciniform carbon.

Table A13. Aciniform Carbon (AC)/Soot Values from the Cretaceous-Tertiary (K-Pg) Boundary

Site	Carbon (mg/cm^2)	AC/soot (%)	AC/soot (g/cm^2)
Agost	3.6	2	.00007
Caravaca	10	14	.00140
Chancet Rocks	35	68	.02380
El Kef	15	19	.00285
Elendgraben	.8	12	.00010
Flaxbourne River	1.3	55	.00072
Gubbio	13	17	.00221
Raton	4	1	.00004
Stevns Klint	11	21	.00231
Sumbar	13	15	.00195
Woodside Creek	4.8	69	.00331
Mean	10.1		.00352
Standard deviation	9.7		.00682

Note. K-Pg carbon fraction (not AC/soot) at 11 sites, and the percent AC/soot at each site. Data are from Wolbach et al. (1990); see that work for data qualifications. Because some values are not well determined, these calculations are estimates.

Supplemental Text

Biomass-Burning Proxies Found at YDB Sites

Following are brief descriptions of reported YDB biomass-burning proxies, all or most of which were found at each YDB site investigated. The first proxy, charcoal, is a common by-product of all wildfires, whether impact related or not, but in impact events, charcoal may take unusual forms. For example, as shown in figure A1, pieces of charcoal from the YDB layer in Pennsylvania and South Carolina were found embedded in high-temperature meltglass (>1200°C; Bunch et al. 2012). The temperatures required to produce YDB spherules and meltglass composed of molten iron and silica (1500°–2100°C) are high enough to initiate biomass burning on contact, supporting the hypothesis that the YDB impact initiated at least local biomass burning. Such material cannot be produced by typical wildfires, in which temperatures are too low to form meltglass (Bunch et al. 2012). Meltglass containing organic material can be produced by volcanism, when lava flows across vegetation, but that origin can be ruled out for YDB sites, because these meltglass samples have nonvolcanic compositions (Bunch et al. 2012). Meltglass that contains organic material, similar to that shown in figure A1, has been reported for known impact events (Schultz et al. 2014).

Carbon Spherules

These are black, vesicular, rounded-to-spherical objects, typically with cracked and patterned surfaces, a thin rind, and honeycomb-like (spongy) interiors (Firestone et al. 2007; Israde-Alcántara et al. 2012; fig. A2). Laboratory experiments previously conducted by coauthors of this article suggest that these carbon-rich spherules were produced from airborne droplets of burning coniferous tree sap (Israde-Alcántara et al. 2012), contrary to the erroneous assertion by Scott et al. (2017) that the laboratory-produced spherules in question were composed of aluminosilicate glass. It is important to note that carbon spherules are not exclusively associated with cosmic impacts but are also produced during normal wildfires (Firestone et al. 2007). Carbon spherules are often present throughout stratigraphic profiles but are invariably at the highest abundance in the YDB. Also, they are typically better preserved in the YDB, possibly because of high-temperature induration during formation.

Scott et al. (2010, 2017) and van Hoesel et al. (2012) argued that YDB carbon spherules and glass-like carbon are unlikely to be impact related, because they formed at low temperatures. However, evidence from the Tunguska and Cretaceous-Tertiary boundary (formerly KTB, now K-Pg) impact events indicates that low-temperature, impact-related fires were common (Florenskiy 1965; Svetsov 2008). Even so, Scott et al. (2017) agree that their evidence does not rule out an impact event, stating that "carbonaceous materials from [the YDB layer at] Arlington Canyon do not . . . in some cases, preclude such an event" (p. 45).

Nanodiamonds in Carbon Spherules

Nanodiamonds were found inside and on the surfaces of two YDB biomass-burning proxies, carbon spherules and glass-like carbon (fig. A3), indicating that nanodiamond formation is associated with YDB impact-related biomass burning. In a search of more than half-a-dozen modern nonimpact wildfires, no nanodiamonds have ever been detected in sediment, carbon spherules, and/or glass-like carbon, suggesting that they form only during impact events. One distinguishing characteristic of YDB carbon spherules is that usually only ~5% (occasionally up to ~50%) contain nanodiamonds, which were observed at every YDB site tested for carbon spherules. In contrast, nanodiamonds have not been observed in carbon spherules from five modern wildfires (Firestone et al. 2007; Israde-Alcántara et al. 2012; Kinzie et al. 2014).

The formation mechanism is currently unclear but possibly involves flash heating and hypoxic atmospheric conditions (Kinzie et al. 2014). Investigating that hypothesis, Israde-Alcántara et al. (2012) reported lab experiments that produced nanodiamonds when carbon spherules were exposed to temperatures of ≥1200°C in an oxygen-deficient atmosphere, as is expected to occur during impact events but does not occur during typical terrestrial wildfires. The association of nanodiamonds with carbon spherules is inconsistent with the claim by Scott et al. (2010, 2017) that all carbon spherules are simply normally charred fungal sclerotia or insect fecal pellets, because there is no known mechanism by which nanodiamonds could form in such material other than by impact (Kinzie et al. 2014). The laboratory tests indicate that the formation of nanodiamonds requires hypoxia and high temperatures, conditions that are not present in typical wildfires (Kinzie et al. 2014). Tian et al. (2011) and Bement et al. (2014) confirmed peak abundances of nanodiamonds in the YDB layer but found no nanodiamonds in carbon spherules or sediment above or below the YDB. This counters the assertion by Daulton et al. (2016) that there is no YDB peak in nanodiamonds, even though that group acknowledges that "there is evidence of cubic nanodiamonds in Late Pleistocene sediments" (p. 28).

Glass-Like Carbon

This is a black, brittle, glassy, often vesicular material that sometimes grades into charcoal (fig. A4; Firestone et al. 2007). Experiments reveal that, like carbon spherules, glass-like carbon is the by-product of burning coniferous tree sap (Israde-Alcántara et al. 2012). The material is common in the YDB layer but also is produced in most natural wildfires and is not unique to the YDB layer. When present, YDB glass-like carbon sometimes contains nanodiamonds (Firestone et al. 2007; Tian et al. 2011; Israde-Alcántara et al. 2012; Kinzie et al. 2014).

Aciniform Carbon

Aciniform carbon, a by-product of all biomass burning, is also an important proxy for known impact events, including the Sudbury (Bunch et al. 1999), Mjølnir (Dypvik et al. 2008), Manson (Varricchio et al. 2009), and K-Pg impacts (Wolbach et al. 1985; Wolbach and Anders 1989; Wolbach 1990). In our work, the terms "soot" and "aciniform carbon" are used interchangeably for simplicity and for consistency with previous work by Wolbach. Aciniform carbon, referred to

here as "AC/soot," is a subset of the broader term, "soot," which is itself a subset of black carbon that includes varying percentages of both aciniform and amorphous carbon (fig. A5). The term soot includes all particulates collected above a flame in a fire, whereas AC/soot consists of only chain-like aggregates of 10–30 spherical units having diameters of 10–50 nm each. More specifically, AC/soot forms when vaporized carbon atoms condense directly from the gas phase to the solid phase above a flame, forming a characteristic "bunch-of-grapes" morphology. These units form necklace-like chains that appear as "clusters of grapes," the definition of "aciniform" and sometimes called "botryoidal," with each sphere containing ~10^5 carbon atoms (Calcote 1981; Harris and Weiner 1985; Kroto 1988). Because of its distinctive morphology, AC/soot can be readily identified.

Along with charcoal, organic carbon, and black carbon, AC/soot can be subject to bioassimilation and/or oxidation over short time spans. It is less susceptible to degradation when deposited by wind or water under chemically reducing conditions and is even more likely to survive when deposited under anoxic conditions. When compacted, AC/soot has a density of 1.76–1.90 g/cm^3 (Long et al. 2013), but in powder form, it is light and "fluffy" and is readily transported through the atmosphere. Because it is slightly hydrophobic, as a result of resins or other plant materials, AC/soot floats and hence is readily distributed by flowing water. The geographic distribution of AC/soot and other particulate matter from a biomass-burning event, including the YDB impact, depends on the atmospheric altitude reached and wind direction/velocity, as is the case for tephra from explosive volcanic eruptions.

Aciniform carbon is rarely found in sedimentary rocks because its high surface-to-volume ratio leads to eventual oxidation. One possible reason why AC/soot was preserved in such widespread abundance at the K-Pg boundary is that the AC/soot was rapidly buried by a blanket of global impact ejecta, which protected it from oxidative attack (e.g., from bacteria and dissolved oxygen in the water column), a phenomenon not observed at the YDB. As a result, absence of AC/soot does not necessarily indicate lack of fires, but its presence is unusual, especially when abundant. If AC/soot from natural fires is not present in sediments or rocks, it is probably because the AC/soot was destroyed before burial or was deposited under chemically oxidizing conditions. Wolbach and Mitra (coauthors of this work) searched extensively for AC/soot in hundreds of samples dating from recent times to several billion years ago, some of which were associated with known impacts. Little to none was present in the nonimpact layers, whereas impact-related sediments frequently contained abundant AC/soot (Wolbach et al. 1985; Wolbach and Anders 1989; Wolbach 1990; Maiorana-Boutilier et al. 2016). This AC/soot most likely resulted from two sources: (1) combustion of biomass, hydrocarbons, and/or carbon-rich minerals (e.g., carbonates) present near the airburst/impact site and (2) combustion of distal biomass ignited by molten ejecta. Biomass burning associated with impact events results in greater abundances and wider distribution of AC/soot than that for normal fires. The AC/soot forms at variable temperatures, but when formed at higher temperatures it is more refractory and durable (Wolbach et al. 1985; Wolbach and Anders 1989; Wolbach 1990). Impacts create favorable conditions, including rapid burial of AC/soot that protects it from physical degradation, bioassimilation, and/or migration through permeable sediment.

Black-Mat Layers

Haynes (2008) investigated organic-rich sedimentary layers, known as "black mats," that are typically dark gray to black because of high organic carbon content (up to ~8%). Haynes (2008) also applied the term "black mat" to coeval layers that are white or light gray. Black-mat sediments typically contain a variable mix of charcoal, woody material, amorphous carbon, and algal remains. Haynes proposed that black mats formed under moist conditions when water tables were higher, allowing enhanced preservation of organics.

Although black mats occur in both younger- and older-than-YDB sequences, these are not as widely distributed as the YD-onset black mats, which are present at ~30% of YDB sites. In addition, YD black mats are the only ones known to be associated with a major climatic perturbation. The YDB impact hypothesis proposes that black mats formed from organic matter and minerals released by impact-related processes, including increased biomass burning and biotic degradation.

The crucial distinguishing factor between nonimpact black mats and impact-related ones is that the latter are invariably associated with impact-related proxies. Thus, the presence of non-YDB black mats is not an argument against the formation of black mats by a cosmic-impact event, as suggested by Pigati et al. (2012), because the latter contain impact-related proxies.

The YD episode type region is northern Europe, where Mangerud (1974) first identified this distinctive period of climate change. In Europe, black mats with evidence of biomass-burning appear as a thin layer at the top of the Usselo

Formation, which marks the transition between the older Allerød warm episode and the cold YD episode, as discussed by van der Hammen and van Geel (2008) and van Hoesel et al. (2012). Widely distributed across the Netherlands, Germany, Belgium, the United Kingdom, France, and Poland, this charcoal-rich, biomass-burning layer co-occurs with YDB cosmic-impact proxies (Firestone et al. 2007).

Altogether, the impact-proxy-rich YDB layer, with an age range of ~12,835–12,735 cal BP, has been found at ~40 sites across three continents. The layer contains abundance peaks in a variable mix of combustion-related markers, including charcoal, carbon spherules, glass-like carbon, AC/soot, PAHs, and fullerenes, which are also associated with the K-Pg boundary impact layer (Wolbach 1990; Belcher et al. 2003; Adatte et al. 2005). For more details and references concerning these proxies, see fig. A8 and tables A1–A4.

Sources of Data

Data for most lakes are from the Global Charcoal Database (GCD 2013). Sources of data are listed in tables A3 and A10. Influx graphs for 35 North American lake-core records are in Marlon et al. (2009). For graphs of many other records in the Global Charcoal Database (GCD 2013), see Power et al. (2008) and the Global Palaeofire website: http://www.bridge.bris.ac.uk/projects/QUEST_IGBP_Global_Palaeofire_WG/database.html.

Charcoal Record Selection

In this study, lake and marine records considered acceptable for computations are limited to those with ages ≥10,000 cal BP and ≤15,000 cal BP and containing at least one sample dating between 13,400 and 12,300 cal BP, spanning the YDB. We also required lake records with published ^{14}C dates, depths, and charcoal/soot values recorded either as concentrations or as influx. Data for 35 lakes are from independent publications (table A8), and most other records are from the Global Charcoal Database (Power et al. 2008; GCD 2013). These sources contain ~680 charcoal records, of which 104 met our selection criteria. Occasionally, ^{14}C dates in the GCD were incorrectly recorded as calibrated ages and vice versa, and in these cases, we used original dates from source publications. In a few cases, GCD depth data conflicted with those in the source publications, and if so, we used the latter. For 23 sites known to exhibit the YDB layer, data were obtained from previous studies (tables A1–A3). Sources and selection criteria for data used in this study are given in "Sources of Data" above.

Extraction of AC/Soot from Sediments

General Information

Aciniform carbon (AC/soot) is composed of units with hexagonal structures that are similar to graphite and have a C:H ratio of about 8–12:1 (Medalia et al. 1983). Anthropogenic AC/soot is termed "carbon black" and is composed of >97% AC/soot (Watson and Valberg 2001). Depending on the conditions of the fire, soot may include varying percentages of AC/soot and amorphous carbon, as discussed below and in "Utilizing YDB Platinum (Pt) as a Datum" in the main text. According to Harris and Weiner (1985), the AC/soot structure is observed whether the AC/soot is generated in a Bunsen burner, a diesel engine, or a fire fueled by natural biomass. However, according to Medalia et al. (1983), chimney soot from domestic wood or coal fires contains very little AC/soot, while in diesel soot the solid particulates are essentially all AC/soot. Hays and Vander Wal (2007) and Wolbach et al. (1985; also Wolbach and Anders 1989 and this study) contradicted the claim that wood fires contain very little AC/soot, after they collected soot derived from such fires and examined its morphology with SEM. Most of the soot that they found consisted of AC/soot that they reported to be similar to that found at the K-Pg boundary, but somewhat different (e.g., Medalia et al. 1983; Watson and Valberg 2001; Gray and Muranko 2006; Buseck et al. 2014).

Because AC/soot is an unequivocal indication of combustion, AC/soot occurrence and quantity were used as definitive evidence for fires at the K-Pg boundary and other cosmic-impact horizons, such as the YDB. In contrast, various processes, including biomass burning and partial diagenesis of organic matter, can produce elemental amorphous carbon in carbon-rich sedimentary rocks. Because the presence of amorphous carbon is not definitive evidence of wildfires, its abundance is ignored during analyses.

AC/Soot Formation and Combustion Conditions

It has been suggested that AC/soot forms by condensation of gaseous carbon in/above a flame directly to the solid (Kroto 1988). The spherical units of AC/soot have a structure similar to that of graphite, consisting of layers of primarily six-membered rings of various lengths occurring in layers of variable spacing (fringe separation), as imaged with transmission electron microscopy (TEM). Production of AC/soot is affected by many variables, including fuel source, O_2 availability, CO_2 concentration above the fire, moisture/humidity of both fuel and air, and temperature of the fire.

Hays and Vander Wal (2007) used TEM to measure the lengths and fringe separation within AC/soot from biomass burning as well as from diesel trucks, oil boilers, and jet aircraft, among others. The authors then compared the statistical distribution of lengths and fringe separations for these combustion products, to identify the source of AC/soot collected in atmospheric aerosols. However, it is not clear that all the variables in AC/soot structure have been understood. For example, how do statistical particle-size distributions change as AC/soot formation temperatures rise? Is O_2 availability controlled for? Is CO_2 permitted to accumulate, and if so, how does this affect AC/soot structure? Is the use of SEM to determine fire temperature and fuel source more or less reliable than using TEM?

Theory and Background: Demineralization, Oxidation, SEM Analysis

Techniques for the separation and identification of elemental carbon from sedimentary rocks were developed for use at the K-Pg boundary (Wolbach et al. 1985; Wolbach and Anders 1989; Wolbach 1990).

Demineralization. Samples are first pulverized to increase surface area and hence the rate of chemical demineralization. Sample mass must be monitored during demineralization. To achieve accuracy, weighing is repeated until masses have stabilized to 0.01 mg. Repeated weighing of original rock samples for previous studies has shown that a standard error of 0.00009 g can be attributed to the masses obtained during this weighing process (W. S. Wolbach, unpublished data, 1996). For all other weighing processes, standard deviations are calculated and assigned as errors. Standard analytical error propagation techniques are used for subsequent calculations.

For the process of demineralization, carbonate, CO_3^{2-}, from limestone or dolostone ($CaCO_3$ or $MgCO_3$, respectively) readily reacts with hydrochloric acid, HCl, producing carbon dioxide and water:

$$2H^+(aq) + CaCO_3(s) \rightarrow H_2O(l) + CO_2(g) + Ca^{2+}(aq). \quad (A1)$$

Silicates in the residue, SiO_4^{-4}, are destroyed with hydrofluoric acid, HF, which attacks the Si-O bonds:

$$SiO_2(s) + 4HF(aq) \rightarrow SiF_4(g) + H_2O(l). \quad (A2)$$

Addition of HF to the residue in the presence of calcium or magnesium ions, however, causes the precipitation of calcium or magnesium fluoride (CaF_2 or MgF_2, respectively), which would contaminate the residue:

$$2F^-(aq) + Ca^{2+}(aq) \rightarrow CaF_2(s). \quad (A3)$$

To prevent this precipitation, the residues must undergo copious rinsing with laboratory-grade deionized water (dH_2O; not the same as distilled water) to minimize Ca^{2+} and Mg^{2+} concentrations in the supernatants after reaction with HCl. Supernatants are tested with small amounts of HF for precipitation of fluorides. If no precipitation occurs, the residues are considered free of Ca^{2+} and Mg^{2+} and are subsequently treated with HF.

Complete demineralization is difficult because of small amounts of relatively inert minerals such as TiO_2 and the slow reactivity of stable silicates such as quartz. This small fraction of minerals is corrected for when elemental carbon components are quantified (see "Particle-Size Analysis and Correction for Minerals and Sample Loss in Postoxidation Residue" below). Residues remaining after demineralization are primarily carbon and are dark brown or black in color, depending on the relative abundance of brown organic carbon and black elemental carbon. Since silicates are tan or white, visual examination for absence of minerals can be used to determine when the samples are adequately demineralized. If significant minerals persist, heavy-liquid density separations can be utilized for removal of these minerals (see "Heavy-Liquid Density Separations" below).

Oxidation. Once demineralization is complete, sample residues are primarily carbonaceous, consisting mainly of organic carbon, kerogen (complex, fossilized organic matter that has undergone some diagenesis), and elemental carbon. To separate organic material from elemental carbon (the component of primary interest, since it includes soot),

residues are oxidized with sodium dichromate, $Na_2Cr_2O_7$, in H_2SO_4 at 50°C, which preferentially destroys organic carbon by converting it to CO_2:

$$2Cr_2O_7^{2-}(aq) + 3C(s) + 16H^+(aq) \rightarrow 8H_2O(l) + 3CO_2(g) + 4Cr^{3+}(aq). \quad (A4)$$

Reaction progress can be monitored through observation of supernatant color. The $Na_2Cr_2O_7/H_2SO_4$ solution is bright orange, while the Cr^{3+} is dark green in solution. The $Na_2Cr_2O_7/H_2SO_4$ solution is replaced upon visual indication of a color change.

Different forms of carbon oxidize at different rates. The oxidation rate of elemental carbon is much slower (half-life [$t_{1/2}$] > 600 h) than that of the most resistant kerogen ($t_{1/2}$ < 180 h) at a constant temperature of 50°C (Wolbach and Anders 1989). Under controlled conditions of a constant temperature of 50°C and a duration of 600 h, most organic carbon and kerogen can be destroyed, while destruction of elemental carbon is minimized (Wolbach and Anders 1989).

Approximately half of the soot carbon is oxidized during this process (Wolbach and Anders 1989). Calculated soot masses must be corrected for this loss by a division factor of 0.48, and an error of 0.05 is assigned to this correction factor (Wolbach and Anders 1989). This correction is as follows:

$$\text{soot mass} = \frac{\text{calculated soot mass}}{0.48 \pm 0.05}. \quad (A5)$$

Some borosilicate glass centrifuge tubes used during the oxidation process can be leached by the $Na_2Cr_2O_7/H_2SO_4$ solution, resulting in negative values for small postoxidation carbon residue masses. Tubes with manufacturer markings and labeling are most susceptible to this process. The labeling is often removed during the etching process because of the elevated temperatures and the effects of the acidic solution. Because visible residue is often present for several samples having these negative values, a correction factor can be applied to all samples in tubes that undergo this leaching. A correction factor of 0.0048 ± 0.0005 g has been determined through repeated examination of K-Pg boundary samples (W. S. Wolbach, unpublished data, 1996; W. S. Wolbach and S. Widicus, unpublished data, 1997; see "Estimated Correction Factor for Leaching of Glass Tubes" below).

SEM Analysis. Characterization of AC/soot and nonaciniform ("nonsoot") portions of the elemental carbon residue is performed with SEM imaging. Anthropogenic carbon black at high magnification has the same characteristic "grape-bunch" morphology as K-Pg AC/soot (Wolbach et al. 1985; Wolbach and Anders 1989). Other forms of coarse carbon such as coal and charcoal are larger, platy particles, sometimes retaining the imprint of cell walls. This coarse carbon often coexists with but is easily distinguishable from soot with SEM imaging.

Micrographs of representative portions of each sample are used to quantify ratios of soot- to nonsoot-particle areas, which are directly proportional to ratios of soot- to nonsoot-particle masses. Under the assumption that all particles are spherical in shape and have uniform density, the area ratio raised to the 1.5 power gives the volumetric ratio of soot to nonsoot particles. This volumetric ratio is then used to calculate relative AC/soot mass. The soot mass is then corrected for loss due to oxidation, and the concentrations of soot and nonsoot components are calculated. A correction for the presence of undissolved minerals can also be determined. A detailed explanation of and derivation of these conversion factors is given in "Particle-Size Analysis and Correction for Minerals and Sample Loss in Postoxidation Residue" below.

AC/Soot Procedure

Materials. All solutions were made with corresponding reagent-grade chemicals purchased from Fisher Scientific. All solutions were made with purified, deionized water (total organic carbon concentration < 2–5 ppb), produced by a Millipore Milli-Q system. Acidic dichromate (sulfochromic) solutions were made with sodium dichromate and concentrated sulfuric acid and then diluted with purified, deionized water. All glass centrifuge tubes used for sample and residue weight determinations were conical to concentrate the small amounts of residue. They were first acid-washed with concentrated HNO_3, washed copiously with distilled water, and then weighed repeatedly to constant weight.

Instrumentation and Equipment. Here is a list of the specific instrumentation and equipment used in the extraction and analysis of soot:

- Labnet HERMLE model Z 400 K centrifuge with swinging buckets;
- Fisher Scientific ultrasonic cleaner, model FS110A;

- VWR Scientific model 1235 PC water bath;
- Lab-Line L-C oven, model 3510;
- Mettler Toledo AT201 analytical balance, with precision to 0.01 mg;
- Millipore Milli-Q Synthesis water purification system with 0.22-μm filter;
- Nunc 30 × 115 mm 50 mL sterile graduated polypropylene centrifuge tubes;
- Kimble 16 × 114 mm 10 mL borosilicate glass centrifuge tubes with conical ends;
- JEOL 5800 LV scanning electron microscope.

Demineralization. Pulverized samples were weighed into prelabeled 50-mL polypropylene graduated conical centrifuge tubes. Excess 9 M HCl was introduced dropwise until most visible reactions ceased. The tubes were capped and the samples mixed thoroughly. The samples remained under acid for 24 h. They were then centrifuged, and supernatants were decanted with disposable polyethylene transfer pipettes. The samples were rinsed thoroughly with dH_2O and centrifuged, and the supernatants were decanted. This process was repeated three times.

After the third rinse, the supernatants were tested for the presence of Ca^{2+} and Mg^{2+} with two drops of 15 M HF/1 M HCl. The absence of precipitation allowed the samples to be treated with excess HF/HCl for 7–10 d. Samples were centrifuged, rinsed twice with dH_2O, and then treated again with 9 M HCl for 24 h. Samples were centrifuged, rinsed twice with dH_2O, and then treated again with HF/HCl. The treatment cycle of HF/HCl and HCl was repeated, ending with HCl, until the sample residue was dark brown or black, indicating that the majority of minerals had been destroyed.

Oxidation. The samples were treated with approximately 30 mL of 0.2 M $Na_2Cr_2O_7$/2 M H_2SO_4 and ultrasonicated until thoroughly mixed, then placed in a 50°C hot water bath. At the first indication of Cr^{3+} production, samples were removed from the water bath and centrifuged, the supernatants were decanted, fresh $Na_2Cr_2O_7/H_2SO_4$ solution was added, and the samples were returned to the water bath. After 600 h, the samples were removed from the hot water bath and centrifuged, and the supernatants were decanted. The samples were rinsed with dH_2O and centrifuged, and the supernatants were decanted. This process was repeated four times. The samples were dried at 110°C, then weighed repeatedly to constant mass.

SEM Analysis. The elemental carbon residue was characterized and soot quantified (if present) with SEM imaging and particle-size analysis ("Particle-Size Analysis and Correction for Minerals and Sample Loss in Postoxidation Residue"). The percentages of soot and nonsoot portions of the elemental carbon residue were calculated and adjusted for loss of soot carbon during the oxidation process. Parts per million of soot and nonsoot portions of the elemental carbon were calculated for each sample.

Heavy-Liquid Density Separations

Some impact-related samples contain significant quantities of acid-resistant minerals. Although extended exposure to HF/HCl treatment will eliminate most silicates, the procedure is time-consuming and often completely ineffective, even at elevated temperatures. Other minerals, such as pyrite or rutile (FeS_2, TiO_2), are resistant to such acid treatments.

Heavy-liquid density separations achieve separation of the mineral components from samples by utilizing the differences between the densities of minerals and carbon components. Small portions (~0.5 g) of the sample are suspended in water by extended ultrasonification. A small amount of high-density liquid (1–2 mL) is placed in a centrifuge tube, and the aqueous sample suspension is gently layered onto this liquid via pipette. After extended centrifugation, the mineral component sinks to the bottom of the high-density liquid, while the carbon sample remains at the interface of the two liquids. The sample component is carefully removed and returned to its original centrifuge tube for rinsing and weighing.

Two methods for this type of separation were successfully developed for the removal of problematic minerals. Aqueous solutions of cesium chloride (CsCl) and sodium metatungstate (SMT) at appropriate densities were found effective in the separation of silicates and pyrite, respectively, from the bulk sample. Successful separation of silicates has been achieved at CsCl solution densities ranging from 1.6 to 1.9 g/mL. Likewise, successful separation of pyrite has been achieved at SMT solution densities ranging from 2.1 to 2.3 g/mL.

Estimated Correction Factor for Leaching of Glass Tubes

Leaching of borosilicate glass centrifuge tubes can occur during dichromate oxidation. Because visible residue was present for several samples yielding negative mass, a correction factor was applied to all samples in tubes that underwent this leaching. This factor has been determined through examination of samples from the DSDP Core project (W. S.

Wolbach, unpublished data, 1996; W. S. Wolbach and S. Widicus, unpublished data 1997). The largest negative value obtained for a tube with visible sample remaining was obtained, and the amount of sample remaining in the tube was estimated. This gave a correction of 6.0 mg. An average of the negative masses of all tubes with no visible sample remaining was obtained independently, leading to a correction of 3.6 mg. These corrections were averaged, yielding a value of 4.8 mg, and a maximum error of 10% was assigned on the basis of visual estimates of carbon present.

Particle-Size Analysis and Correction for Minerals and Sample Loss in Postoxidation Residue

High-mass-number elements appear brighter during SEM characterization than elements of lower mass number. Minerals contain elements of higher mass number and therefore appear brighter than do carbonaceous components of a sample. The relative brightness of particles is used during SEM characterization to distinguish between carbonaceous and noncarbonaceous portions of the sample. Visual estimates of the carbon and noncarbon fractions of the SEM image area can be used to calculate the percentages by volume of carbon and noncarbon portions (of the total particle volume) as follows.

Total Volume Calculations. The total volume of material is composed of soot, nonsoot, and noncarbonaceous minerals, such as rutile, a common mineral in samples from the K-Pg impact, for which this method was developed. The carbonaceous materials present comprise soot and nonsoot:

$$\begin{aligned} V_{\text{total}} &= V_{\text{soot C}} + V_{\text{nonsoot C}} + V_{\text{rutile}}, \\ V_{\text{total}} &= V_{\text{carbon}} + V_{\text{rutile}}, \\ V_{\text{carbon}} &= V_{\text{soot C}} + V_{\text{nonsoot C}}. \end{aligned}$$

Volume of Carbonaceous Material. Each carbon particle (soot and nonsoot) is assumed to be spherical. The cross-sectional area of each particle is measured with ImageJ64. From these measured areas, the radius of each particle is determined. The radius of each particle is then used to calculate the volume of each soot and nonsoot carbon particle. Volumes are summed to determine the total volume of carbonaceous material, both soot and nonsoot:

$$\begin{aligned} A_{\text{sph}} &= \pi r_{\text{sph}}^2 \Rightarrow r_{\text{sph}} \sqrt{\frac{A_{\text{sph}}}{\pi}}, \\ V_{\text{sph}} &= \frac{4}{3}\pi r_{\text{sph}}^2 \Rightarrow V_{\text{sph}} = \frac{4}{3}\pi \left(\sqrt{\frac{A_{\text{sph}}}{\pi}} \right)^3, \\ V_{\text{sph}} &= \frac{4}{3}\pi^{-1/2} A_{\text{sph}}^{3/2}. \end{aligned}$$

For n spherical soot particles,

$$V_{\text{soot C}} = \sum_{i=1}^{n} V_{\text{sph soot C},\, i}.$$

For n spherical nonsoot particles,

$$\mathrm{V}_{\text{nonsoot C}} = \sum_{i=1}^{n} V_{\text{sph nonsoot C},\, i}.$$

Volume of Noncarbonaceous Material (Rutile). Rutile particles are assumed to be cylindrical. The cross-sectional area and width of each rutile particle are measured with ImageJ64. From these measured areas and widths, the volume of each rutile particle is determined. The volumes of rutile particles are summed to determine the total volume of rutile material:

$$\begin{aligned} A_{\text{cyl}} &= w_{\text{cyl}} L_{\text{cyl}} = 2 r_{\text{cyl}} L_{\text{cyl}} \Rightarrow r_{\text{cyl}} L_{\text{cyl}} = \frac{A_{\text{cyl}}}{2}, \\ V_{\text{cyl}} &= \pi r_{\text{cyl}}^2 L_{\text{cyl}} \Rightarrow V_{\text{cyl}} = \pi r_{\text{cyl}} (r_{\text{cyl}} L_{\text{cyl}}), \\ V_{\text{cyl}} &= \frac{\pi r_{\text{cyl}} A_{\text{cyl}}}{2}, \\ V_{\text{cyl}} &= \frac{\pi w_{\text{cyl}} A_{\text{cyl}}}{4}. \end{aligned}$$

For n cylindrical rutile particles,

$$V_{\text{rutile}} = \sum_{i=1}^{n} V_{\text{cyl rutile},\, i}.$$

Mass and Percent Mass of Carbonaceous and Noncarbonaceous (Rutile) Material. Multiplying the percent volume of a material by the total volume of material and then multiplying by the density of that material gives the mass of that material. It is assumed that soot and nonsoot carbonaceous material have equal density ($d = 1.0\ \text{g/cm}^3$) and that rutile has a higher density ($d = 4.23\ \text{g/cm}^3$):

$$\begin{aligned} m_{\text{soot C}} &= V_{\text{soot C}} \times d_{\text{carbon}} = V_{\text{soot C}} \times 1.0\ \text{g/cm}^3, \\ m_{\text{nonsoot C}} &= V_{\text{nonsoot C}} \times d_{\text{carbon}} = V_{\text{nonsoot C}} \times 1.0\ \text{g/cm}^3, \\ m_{\text{rutile}} &= V_{\text{rutile}} \times d_{\text{rutile}} = V_{\text{rutile}} \times 4.23\ \text{g/cm}^3. \end{aligned}$$

Adding the masses of each material gives the total mass of material:

$$m_{\text{total}} = m_{\text{soot C}} + m_{\text{nonsoot C}} + m_{\text{rutile}}.$$

The mass percent of each material is calculated by dividing the mass of each material by the total mass of material and then multiplying by 100:

$$\%m_{\text{soot C}} = \frac{m_{\text{soot C}}}{m_{\text{total}}} \times 100,$$

$$\%m_{\text{nonsoot C}} = \frac{m_{\text{nonsoot C}}}{m_{\text{total}}} \times 100,$$

$$\%m_{\text{rutile}} = \frac{m_{\text{rutile}}}{m_{\text{total}}} \times 100.$$

Soot Weight Percent and Mass. The weight percentage of soot in the residue material is calculated by dividing the mass of soot by the mass of total material (soot, nonsoot, and rutile). Then the dividend is multiplied by 100:

$$\text{wt\% soot} = \frac{m_{\text{soot C}}}{m_{\text{total}}} \times 100.$$

The mass of soot in the residue material is calculated by dividing the weight percentage of soot by 100 and then multiplying by the residue material mass:

$$\text{soot mass (g)} = \frac{\text{wt\% soot}}{100} \times \text{residue mass (g)}.$$

Soot Mass Correction for 600-h Oxidation. The calculated mass of soot in the residue is corrected to account for the oxidation for 600 h at 50°C with 0.1 M $K_2Cr_2O_7$ in 2 M H_2SO_4. After the 600-h oxidation, 52% of soot is lost; thus, the correction is achieved by dividing the calculated soot concentration by 0.48:

$$\text{corrected soot mass (g)} = \frac{\text{soot mass (g)}}{0.48}.$$

Soot Concentrations in Initial Rock Sample. The concentration of soot in parts per million in the initial rock sample is calculated by dividing the calculated corrected mass of soot by the mass of the initial rock sample and multiplying by 1 million:

$$\text{soot concentration (ppm)} = \frac{\text{corrected soot mass (g)}}{\text{inital rock sample mass (g)}} \times 10^6.$$

Platinum Measurements

Activation Laboratories performed platinum analyses, using the 1C-Research protocol (Moore et al. 2017), which combines fire assay and ICP-MS. Samples of ~50–60 g of sediment are required for the 1C-Research analysis; smaller sample sizes were often found to produce inconclusive results. Each sample was mixed with fire-assay fluxes, heated to ~1060°C to form a lead button, and then reheated to produce an Ag doré bead. After multiple steps of acid dissolution, a Perkin Elmer Sciex ELAN 9000 ICP30 mass spectrometer was used to analyze the sample solutions for Au, Pt, and Pd, along with method blanks, sample duplicates, and certified reference materials. Measurements were reported in parts per billion, with a detection limit of 0.1 ppb for Pt. New and previous Pt results from Moore et al. (2017) are given in table A6.

Age-Depth Models

To produce new age-depth models for the lake-core records, we used Bayesian statistical analyses (Bronk Ramsey 1998, 2009; Parnell et al. 2008; Kennett et al. 2015). Bayesian modeling programs are able to (1) calculate millions of possible age models (iterations) and determine the average one (weighted mean), (2) correct any dates in a group that are anomalously young or old, (3) integrate dates with prior nonchronological information (e.g., stratigraphy, archaeology, palynology, and climatology), and (4) use modeling to overcome biases inherent in the age uncertainties of radiocarbon, uranium series, optically stimulated luminescence, and thermoluminescence dating (Bronk Ramsey 1998). Because of these advantages, Bayesian age-depth modeling is considered more robust and flexible than other model types (Bronk Ramsey 2008; Parnell et al. 2008), which has led to its increased use in Bayesian analytical programs for multiple disciplines, for example, BChron (Parnell et al. 2008), BCal (Buck et al. 1999), OxCal (Bronk Ramsey 2008), and Bacon (Blaauw and Christen 2011). For this study, we used both BChron (ver. 3.2) and OxCal (ver. 4.2.4.). We present all output by age at 95% CI.

Bayesian modeling is labor intensive (millions of Bayesian calculations for each site), but using it can minimize some of the weaknesses in lake-core data sets, such as inadequate numbers of high-precision radiocarbon dates. Bayesian modeling is designed so that instead of each data set contributing equally to the final average, higher-quality data contribute more "weight" than others, thus providing more accurate age-depth models (Bronk Ramsey 1998; Parnell et al. 2008; Bronk Ramsey 2009; Kennett et al. 2015). For an example of our Bayesian modeling with the OxCal code, see the next section. In this study, we produced new Bayesian analytical age-depth models, using 8760 data points from 129 lake-core records. Representative charcoal data for selected lakes are shown in figures A10 and A11. The average age span of each lake-core sample is ~83 y, and 72% have age uncertainties of ≤300 y; the average chronological resolution (age uncertainty) is approximately ±179 y (fig. A10; table A9). Data from the late YD and early Holocene (<12,300 cal BP) were not included because anthropogenically caused fires became increasingly common (Cooke 1998; Power et al. 2008), potentially obscuring the natural wildfire record.

Example of Bayesian Age-Depth Code Used in OxCal

The data used are for Surucucho Lake, Ecuador, South America, GCD record 60; radiocarbon dates are from GCD (2013). The "P_Sequence" code is used when depths and dates are available and it is necessary to interpolate ages for undated samples. "Outlier Model" is used to make corrections in samples with outlier dates, that is, those that are either too old or too young for the best statistical model, as determined by OxCal.

```
Options()
{
BCAD=FALSE;
kIterations=90;
};
Plot()
{
//Dates from GCD record #60
Outlier_Model(General,T(5),U(0,3),t);
```

```
P_Sequence(Surucucho Lake,0.1,0.5)
{
Boundary(Base){z=1212.78;Outlier(General,0.5);};
R_Date(Beta-39954,11870,220){z=918.5;Outlier(General,0.5);};
R_Date(Beta-39953,10650,150){z=868.5;Outlier(General,0.5);};
R_Date(Beta-39952,12940,120){z=817.0;Outlier(General,0.5);};
R_Date(Beta-27887,12150,210){z=815.0;Outlier(General,0.5);};
R_Date(Beta-31247,13070,270){z=737.5;Outlier(General,0.5);};
R_Date(Beta-31246,10000,140){z=647.5;Outlier(General,0.5);};
R_Date(Beta-27725,10330,140){z=587.5;Outlier(General,0.5);};
R_Date(Beta-31245,6500,80){z=408.5;Outlier(General,0.5);};
Boundary();
};
};
```

Regression-Lowess Method

We followed the protocol described by Marlon et al. (2009) as follows:

1. *Influx*. Charcoal concentrations (particles/cm^3) were converted to influx values (particles/cm^2/y) by dividing charcoal values by deposition time (y/cm).
2. *Box-Cox transformations*. To stabilize the data variance, the lowest influx value in each record was subtracted from other values and the results were divided by the highest value, after which 0.01 was added, so that all values were >0. The charcoal influx data were then transformed with the Box-Cox transformation, as described in Power et al. (1998).
3. *Z-scores*. To allow comparisons among records that feature widely varying average charcoal influx rates, the transformed values were converted to values called "*Z*-scores" by subtracting the mean value and dividing by the standard deviation.
4. *Lowess smoothing*. Finally, data were lowess-smoothed, typically with 200-y half-windows for lake/marine records and 200–1000 y for ice cores, depending on the number of data points (i.e., fewer data points required larger windows).

Bayesian EIV-Spline Method

Radiocarbon dates were calibrated with IntCal13 in OxCal, version 4.2.4 (Bronk Ramsey 1998, 2009), to produce Bayesian age-depth models; "P_Sequence," "Outlier," "Phase," and "Difference" codes were used. Next, data were converted to *Z*-scores, as described above, and plotted with a new analytical tool designed to run within the R-based Bayesian program BChron (cocreated by A. C. Parnell; Haslett and Parnell 2008; Parnell et al. 2008). The Bayesian EIV algorithm was first developed and used by Cahill et al. (2015).

We used a P-spline ("penalized splines") model set in an EIV framework to describe the nonlinear relationship between charcoal *Z*-scores and chronological ages that have been estimated with uncertainty. The EIV (e.g., Dey et al. 2000) is an approach to regression problems that is used when the predictor variables are measured with error. In this case, our predictor (age) is measured with uncertainty due to the dating techniques that were used. The aim of the EIV approach is to estimate the relationship between charcoal *Z*-scores and the true error-free age.

In the EIV model, we assume that each *Z*-score and age observation is drawn from a bivariate normal distribution, that the means satisfy a relationship in which the expected value of the uncertain age is the true age, and that the expected *Z*-score is a function of age (in this case, a spline smoothing function). Age uncertainties (provided by BChron) and *Z*-score uncertainties (provided by EIV) are included in the variance-covariance function of this bivariate normal distribution. While individual calibrated radiocarbon ages will not satisfy the bivariate normality assumption, when large numbers of dates are taken together the model is robust to non-Gaussianity of the ages, as demonstrated by Parnell and Gehrels (2014).

The spline smoothing functions are produced from B-spline basis functions penalized to produce a smooth curve. These basis functions, which are functions of age, are included in the columns of a design matrix **B**. The **B** columns are predictor variables and were scaled by corresponding fitted parameters and summed to produce fitted values of the smoothed curve. Following the approach outlined by Eilers and Marx (1996), we can choose a relatively large number of B-splines with an additional penalty, *P*, on the scaling parameters. Whereas the large basis would result in overfitting, the penalty forces the coefficients to vary more smoothly. The smoothness can be tuned by changing a smoothness parameter, nseg (representing the number of segments), which ranged from 60 for Asia with (with ~600 data points) to 80 for North America (~6000 data points). Larger data sets required less smoothing and therefore higher nseg values. Parameter values were selected to avoid both oversmoothing, which would result in significant loss of detail, and undersmoothing, which would make the composite curve susceptible to the influence of individual data points. Use of different nseg values did not affect the conclusions. This EIV P-spline approach provides a flexible model for capturing the nonlinear relationship between charcoal *Z*-scores and uncertain age. The EIV routine creates plots showing uncertainties of *Z*-scores at 68% and 95% CIs. The program also generates a Results.csv file that contains age uncertainties for each *Z*-score. The BChron and EIV code we used can be obtained from coauthor A. C. Parnell at https://maths.ucd.ie/~parnell_a/.

REFERENCES CITED ONLY IN THE APPENDIX

Anderson, R. 2005. Contrasting vegetation and fire histories on the Point Reyes Peninsula during the pre-settlement and settlement periods. Flagstaff, Center for Environmental Sciences and Education and the Quaternary Sciences Program, Northern Arizona University, 31 p.

Andric, M. 2011. Late Glacial vegetation at Lake Bled and Griblje Marsh (Slovenia): a comparison of (in last glacial maximum) glaciated and non-glaciated landscapes *In* Toškan, B., ed. Fragments of Ice Age environments: proceedings in honour of Ivan Turk's jubilee. Opera Inst. Archaeol. Slov. 21:235–249.

Andronikov, A. V.; Andronikova, I. E.; Loehn, C. W.; Lafuente, B.; Ballenger, J. A.; Crawford, G. T.; and Lauretta, D. S. 2016*a*. Implications from chemical, structural and mineralogical studies of magnetic microspherules from around the lower Younger Dryas boundary (New Mexico, USA). Geogr. Ann. Ser. A Phys. Geogr. 98:39–59.

Andronikov, A. V.; Lauretta, D. S.; Andronikova, I. E.; and Maxwell, R. J. 2011. On the possibility of a late Pleistocene extraterrestrial impact: LA-ICP-MS analysis of the black mat and Usselo Horizon samples. Meteoritics Planet. Sci. 46(suppl.):A11.

Baker, D. W.; Miranda, P. J.; and Gibbs, K. E. 2008. Montana evidence for extra-terrestrial impact event that caused Ice-Age mammal die-off. EOS: Trans. Am. Geophys. Union 89(23), Joint Assembly suppl., abstract P41A-05.

Ballard, J. P., and Lowell, T. V. 2009. A Lateglacial paleofire record for east-central Michigan focusing on the Gainey archaeological site. *In* Annual Meeting, 43rd (Rockford, IL, 2009), Geological Society America, North-Central Section, paper 24-7.

Beaty, R. M., and Taylor, A. H. 2008. A 14,000-year sedimentary charcoal record of fire from the northern Sierra Nevada, Lake Tahoe Basin, California, USA. Holocene 19:347–358.

Becker, L.; Poreda, R.; Kennett, J. P.; Kennett, D. J.; Erlandson, J. M.; and West, A. 2009. Wildfires, soot and fullerenes in the 12,900 ka Younger Dryas boundary layer in North America. EOS: Trans. Am. Geophys. Union 90(52), Fall Meeting suppl., abstract PP31D-1393.

Beets, C.; Sharma, M.; Kasse, K.; and Bohncke, S. 2008. Search for extraterrestrial osmium at the Allerod–Younger Dryas boundary. EOS: Trans. Am. Geophys. Union 89(53), Fall Meeting suppl., abstract V53A-2150.

Bement, L. C.; Madden, A. S.; Carter, B. J.; Simms, A. R.; Swindle, A. L.; Alexander, H. M.; Fine, S.; and Benamara, M. 2014. Quantifying the distribution of nanodiamonds in pre–Younger Dryas to recent age deposits along Bull Creek, Oklahoma Panhandle, USA. Proc. Natl. Acad. Sci. USA 111(5):1726–1731.

Boslough, M.; Nicoll, K.; Holliday, V.; Daulton, T. L.; Meltzer, D.; Pinter, N.; Scott, A. C.; et. al. 2012. Arguments and evidence against a Younger Dryas impact event. *In* Giosan, L.; Fuller, D. Q.; Nicoll, K.; Flad, R. K.; and Clift, P. D., eds. Climates, landscapes, and civilizations. Geophys. Monogr. Ser. 198. Washington, DC, American Geophysical Union, p. 13–26.

Boyd, M.; Running, G. L., IV; and Havholm, K. 2003. Paleoecology and geochronology of glacial Lake Hind during the Pleistocene-Holocene transition: a context for Folsom surface finds on the Canadian prairies. Geoarchaeology 18:583–607.

Briles, C. E. 2008. Holocene vegetation and fire history of the floristically diverse Klamath Mountains, northern California, USA. PhD dissertation, University of Oregon, Eugene.

Bronk Ramsey, C. 2008. Deposition models for chronological records. Quat. Sci. Rev. 27(1–2):42–60.

Bunch, T. E.; Becker, L.; Des Marais, D.; Tharpe, A.; Schultz, P. H.; Wolbach, W.; Glavin, D. P.; Brinton, K. L.; and Bada, J. L. 1999. Carbonaceous matter in the rocks of the Sudbury Basin, Ontario, Canada. *In* Dressler, B. O., and V. L. Sharpton, V. L., eds. Large meteorite impacts and planetary evolution II. Geol. Soc. Am. Spec. Pap. 339:331–343.

Buseck, P. R.; Adachi, K.; Gelencsér, A.; Tompa, É.; and Pósfai, M. 2014. A material-based term for strongly light-absorbing Carbonaceous particles. Aerosol Sci. Technol. 48:777–788.

Calcote, H. F. 1981. Mechanisms of soot nucleation in flames—a critical review. Combust. Flame 42:215–242.

Carcaillet, C., and Richard, P. J. H. 2000. Holocene changes in seasonal precipitation highlighted by fire incidence in eastern Canada. Clim. Dyn. 16:549–559.

Cooke, R. 1998. Human settlement of Central America and northernmost South America (14,000–8000 BP). Quat. Int. 49–50:177–190.

Daulton, T. L.; Amari, S.; Scott, A. C.; Hardiman, M.; Pinter, N.; and Anderson, R. S. 2016. Comprehensive analysis of nanodiamond evidence relating to the Younger Dryas impact hypothesis. J. Quat. Sci. 32:7–34.

Daulton, T. L.; Pinter, N.; and Scott, A. C. 2010. No evidence of nanodiamonds in Younger-Dryas sediments to support an impact event. Proc. Natl. Acad. Sci. USA 107(37):16,043–16,047.

Davis, O. K., and Shafer, D. S. 1992. A Holocene climatic record for the Sonoran Desert from pollen analysis of Montezuma Well, Arizona, USA. Palaeogeogr. Palaeoclimatol. Palaeoecol. 92:107–119.

Dey, D. K.; Ghosh, S. K.; and Mallick, B. K. 2000. Generalized linear models: a Bayesian perspective. New York, Dekker.

Domínguez-Vázquez, G. 2012. Paleoenvironmental conditions at the Bajio during the last glacial maximum. Cordilleran Section Annual Meeting, 108th (Querétaro, Mexico). Geol. Soc. Am. Abstr. Programs 44(3):55.

Dypvik, H.; Wolbach, W. S.; Shuvalov, V.; and Widicus Weaver, S. L. 2008. Did the Mjølnir asteroid impact ignite Barents Sea hydrocarbon source rocks? *In* Evans, K. R.; Horton, J. W., Jr.; King, D. T.; and Morrow, J. R., eds. The sedimentary record of meteorite impacts. Geol. Soc. Am. Spec. Pap. 437:65–72.

Earle, C. J.; Brubaker, L. B.; and Anderson, P. M. 1996. Charcoal in northcentral Alaskan lake sediments: relationships to fire and late-Quaternary vegetation history. Rev. Palaeobot. Palynol. 92:83–95.

Eilers, P. H. C., and Marx, B. D. 1996. Flexible smoothing with B-splines and penalties. Stat. Sci. 11(2):89–121.

Erlandson, J. M. 2007. Sea change: the Paleocoastal occupations of Daisy Cave. *In* Neusius, S. W., and Gross, G. T., eds. Seeking our past: an introduction to North American archaeology. Oxford, Oxford University Press, p. 135–143.

Erlandson, J. M.; Kennett, D. J.; Ingram, B. L.; Guthrie, D. A.; Morris, D. P.; Tveskov, M. A.; West, G. J.; and Walker, P. L. 1996. An archaeological and paleontological chronology for Daisy Cave (CASMI-261), San Miguel Island, California. Radiocarbon 38:355–373.

Fayek, M.; Anovitz, L. M.; Allard, L. F.; and Hull, S. 2012. Framboidal iron oxide: chondrite-like material from the black mat, Murray Springs, Arizona. Earth Planet. Sci. Lett. 319–320:251–258.

Firestone, R. B. 2009. The case for the Younger Dryas extraterrestrial impact event: mammoth, megafauna, and Clovis extinction, 12,900 years ago. J. Cosmol. 2:256–285.

Firestone, R. B.; West, A.; Revay, Z.; Hagstrum, J. T.; Belgya, T.; Smith, A. R.; Que Hee, S. S.; and Smith, A. R. 2010. Analysis of the Younger Dryas impact layer. J. Sib. Fed. Univ. Eng. Technol. 1(3):30–62.

Flannigan, M. D.; Campbell, I. D.; Wotton, B. M.; Carcaillet, C.; Richard, P.; and Bergeron, Y. 2001. Future fire in Canada's boreal forest: palaeoecology results and general circulation model—regional circulation model simulations. Can. J. For. Res. 31:854–864.

Fuller, J. L. 1997. Holocene forest dynamics in southern Ontario, Canada: fine-resolution pollen data. Can. J. Bot. 75:1714–1727.

Gage, J. A. 2008. Forest disturbance history in the Sawtooth Mountains of central Idaho and the Beaverhead Range of western Montana. MS thesis, Montana State University, Bozeman, 154 p.

Ge, T.; Courty, M. M.; and Guichard, F. 2009. Field-analytical approach of land-sea records for elucidating the Younger Dryas boundary syndrome. EOS: Trans. Am. Geophys. Union 90(52), Fall Meeting suppl., abstract PP31D-1390.

Goodyear, A. C. 1999. The early Holocene occupation of the southeastern United States: a geoarchaeological summary. *In* Bonnichsen, R., and Turnmire, K., eds. Ice Age peoples of North America: environments, origins, and adaptations of the first Americans. Corvallis, OR, Center for the Study of the First Americans, p. 432–481.

———. 2005. Evidence of pre-Clovis sites in the eastern United States. *In* Bonnichsen, R.; Lepper, B. T.; Stanford, D.; and Waters, M. R., eds. Paleoamerican origins: beyond Clovis. College Station, TX, Center for the Study of the First Americans, p. 103–112.

———. 2006. Recognizing the Redstone fluted point in the South Carolina Paleoindian point data base. Curr. Res. Pleistocene 23:100–103.

———. 2010. Instrument-assisted fluting as a technochronological marker among North American Paleoindian points. Curr. Res. Pleistocene 27:86–88.

———. 2013. Update on the 2012–2013 activities of the Southeastern Paleoamerican Survey. Legacy (newsletter of the South Carolina Institute of Archaeology and Anthropology) 17(1):10–12.

Goodyear, A. C.; Miller, S.; and Smallwood, S. 2007. Introducing Clovis at the Topper site, 38AL23, Allendale County, South Carolina. *In* Annual meeting of the Society for American Archaeology, 72nd (Austin, TX, 2007), Abstracts, p. 178.

Goodyear, A. C., and Steffy, K. 2003. Evidence of a Clovis occupation at the Topper site, 38AL23, Allendale County, South Carolina. Curr. Res. Pleistocene 20:23–25.

Gray, C. A., and Muranko, H. 2006. Studies of robustness of industrial aciniform aggregates and agglomerates—carbon black and amorphous silicas: a review amplified by new data. J. Occup. Environ. Med. 48:1279–1290.

Han, Y. M.; Peteet, D. M.; Arimoto, R.; Cao, J. J.; An, Z. S.; Sritrairat, S.; and Yan, B. Z. 2016. Climate and fuel controls on North American paleofires: smoldering to flaming in the Late-Glacial–Holocene transition. Sci. Rep. 6:20719. doi:10.1038/srep20719.

Harris, S. J., and Weiner, A. M. 1985. Chemical kinetics of soot particle growth. Annu. Rev. Phys. Chem. 36:31–52.

Haynes, C. V., Jr. 2007. Appendix B: nature and origin of the black mat, stratum F_2. *In* Haynes, C. V., Jr., and Huckell, B. B., eds. Murray Springs: a Clovis site with multiple activity areas in the San Pedro Valley, Arizona. Tucson, University of Arizona Press, p. 240–249.

Haynes, C. V., Jr.; Boerner, J.; Domanik, K.; Lauretta, D.; Ballenger, J.; and Goreva, J. 2010. The Murray Springs Clovis site, Pleistocene extinction, and the question of extraterrestrial impact. Proc. Natl. Acad. Sci. USA 107(9):4010–4015.

Hays, M. D., and Vander Wal, R. L. 2007. Heterogeneous soot nanostructure in atmospheric and combustion source aerosols. Energy Fuels 21:801–811.

Israde-Alcántara, I.; Bischoff, J. L.; Domínguez-Vázquez, G.; Li, H.-C.; DeCarli, P. S.; Bunch, T. E.; Wittke, J. H.; et. al. 2012. Evidence from central Mexico supporting the Younger Dryas extraterrestrial impact hypothesis. Proc. Natl. Acad. Sci. USA 109: E738–E747.

Jodry, M. A.; Shafer, D. S.; Sanford, D. J.; and Davis, O. K. 1989. Late Quaternary environments and human adaptation in the San Luis Valley, south-central Colorado. *In* Harmon, E. J., ed. Water in the valley: a 1989 perspective on water supplies, issues, and solutions in the San Luis Valley, Colorado. Eighth Annual Field Trip Guidebook. Lakewood, Colorado Groundwater Association, p. 189–208.

Kennett, D. J.; Kennett, J. P.; West, A.; Mercer, C.; Que Hee, S. S.; Bement, L.; Bunch, T. E.; Sellers, M.; and Wolbach, W. S. 2009*a*. Nanodiamonds in the Younger Dryas boundary sediment layer. Science 323:94.

Kennett, D. J.; Kennett, J. P.; West, A.; West, G. J.; Bunch, T. E.; Culleton, B. J.; Erlandson, J. M.; et. al. 2009*b*. Shock-synthesized hexagonal diamonds in Younger Dryas boundary sediments. Proc. Natl. Acad. Sci. USA 106:12,623–12,628.

Kneller, M., and Peteet, D. 1999. Late-glacial to early Holocene climate changes from a central Appalachian pollen and macrofossil record. Quat. Res. 51:133–147.

Kring, D. A., and Durda, D. D. 2003. The day the world burned. Sci. Am. 289(6):98–105.

Kroto, H. 1988. Space, stars, C_{60}, and soot. Science 242:1139–1145.

Kurbatov, A. V.; Mayewski, P. A.; Steffensen, J. P.; West, A.; Kennett, D. J.; Kennett J. P.; Bunch, T. E.; et. al. 2010. Discovery of a nanodiamond-rich layer in the Greenland ice sheet. J. Glaciol. 56:747–757.

LeCompte, M. A.; Goodyear, A. C.; Demitroff, M. N.; Batchelor, D.; Vogel, E. K.; Mooney, C.; Rock, B. N.; and Seidel, A. W. 2012. Independent evaluation of conflicting microspherule results from different investigations of the Younger Dryas impact hypothesis. Proc. Natl. Acad. Sci. USA 109:E2960–E2969.

Lininger, K. 2007. A late Pleistocene/early Holocene fire record from Appleman Lake, Indiana: the use of charcoal analysis in investigating landscape change. BS thesis, University of Wisconsin–Madison.

Long, C. M.; Nascarella, M. A.; and Valberg, P. A. 2013. Carbon black vs. black carbon and other airborne materials containing elemental carbon: physical and chemical distinctions. Environ. Pollut. 181:271–286.

Mahaney, W. C.; Kalm, V.; Krinsley, D. H.; Tricart, P.; Schwartz, S.; Dohm, J.; Kim, K. J.; et. al. 2010*a*. Evidence from the northwestern Venezuelan Andes for extraterrestrial impact: the black mat enigma. Geomorphology 116(1–2):48–57.

Mahaney, W. C., and Keiser, L. 2012. Weathering rinds: unlikely host clasts for an impact-induced event. Geomorphology 184:74–83.

Mahaney, W. C.; Keiser, L.; Krinsley, D. H.; Pentlavalli, P.; Allen, C. C. R.; Somelar, P.; Schwartz, S.; et. al. 2013. Weathering rinds as mirror images of palaeosols: examples from the Western Alps with correlation to Antarctica and Mars. J. Geol. Soc. Lond. 170:833–847. doi:10.1144/jgs2012-150.

Mahaney, W. C., and Krinsley, D. 2012. Extreme heating events and effects in the natural environment: implications for environmental geomorphology. Geomorphology 139–140:348–359.

Mahaney, W. C.; Krinsley, D.; and Kalm, V. 2010*b*. Evidence for a cosmogenic origin of fired glaciofluvial beds in the northwestern Andes: correlation with experimentally heated quartz and feldspar. Sediment. Geol. 231(1–2):31–40.

Mahaney, W. C.; Krinsley, D. H.; Kalm, V.; Langworthy, K.; and Ditto, J. 2011*a*. Notes on the black mat sediment, Mucuñuque catchment, northern Mérida Andes, Venezuela. J. Adv. Microsc. Res. 6(3):177–185.

Mahaney, W. C.; Krinsley, D.; Langworthy, K.; Kalm, V.; Havics, T.; Hart, K. M.; Kelleher, B. P.; Schwartz, S.; Tricart, P.; and Beukens, R. 2011*b*. Fired glaciofluvial sediment in the northwestern Andes: biotic aspects of the black mat. Sediment. Geol. 237(1–2):73–83.

Mahaney, W. C.; Somelar, P.; Dirszowsky, R. W.; Kelleher, B.; Pentlavalli, P.; McLaughlin, S.; Kulakova, A. N.; et. al. 2016*a*. A microbial link to weathering of postglacial rocks and sediments, Mount Viso area, Western Alps, demonstrated through analysis of a soil/paleosol bio/chronosequence. J. Geol. 124:149–169.

Mangerud, J.; Andersen, S. T.; Berglund, B. E.; and Donner, J. J. 1974. Quaternary stratigraphy of Norden, a proposal for terminology and classification. Boreas 3:109–128.

Marshall, W.; Head, K.; Clough, R.; and Fisher, A. 2011. Exceptional iridium concentrations found at the Allerød–Younger Dryas transition in sediments from Bodmin Moor in southwest England. International Union for Quaternary Research Congress, 18th (Bern, Switzerland, 2011), paper 2641.

Medalia, A. I.; Rivin, D.; and Sanders, D. R. 1983. A comparison of carbon black with soot. Sci. Total Environ. 31:1–22.

Melott, A.; Thomas, B. C.; Dreschhoff, G.; and Johnson, C. K. 2010. Cometary airbursts and atmospheric chemistry: Tunguska and a candidate Younger Dryas event. Geology 38:355–358. doi:10.1130/G30508.1.

Mentlík, P.; Minár, J.; Břízová, E.; Lisá, L.; Tábořík, P.; and Stacke, V. 2010. Glaciation in the surroundings of Prášilské Lake (Bohemian Forest, Czech Republic). Geomorphology 117(1–2):181–194.

Paquay, F. S.; Goderis, S.; Ravizza, G.; Vanhaeck, F.; Boyd, M.; Surovell, T.; Holliday, V. T.; Haynes, C. V., Jr.; and Claeys, P. 2009. Absence of geochemical evidence for an impact event at the Bølling–Allerød/Younger Dryas transition. Proc. Natl. Acad. Sci. USA 106(51):21,505–21,510. doi:10.1073/pnas.0908874106.

Parnell, A. C., and Gehrels, W. R. 2014. Using chronological models in late Holocene sea-level reconstructions from salt marsh sediments. *In* Shennan, I.; Horton, B. P.; and Long, A. J., eds. Handbook of sea-level research. Chichester, Wiley-Blackwell, p. 500–513.

Petaev, M. I.; Huang, S.; Jacobsen, S. B.; and Zindler, A. 2013*a*. Large platinum anomaly in the GISP2 ice core: evidence for a cataclysm at the Bølling-Allerød/Younger Dryas Boundary? Lunar and Planetary Science Conference, 44th (The Woodlands, TX, 2013), abstract 1046.

Pigati, J. S.; Latorre, C.; Rech, J. A.; Betancourt, J. L.; Martínez, K. E.; and Budahn, J. R. 2012. Accumulation of impact markers in desert wetlands and implications for the Younger Dryas impact hypothesis. Proc. Natl. Acad. Sci. USA 109(19):7208–7212.

Pinter, N.; Scott, A. C.; Daulton, T. L.; Podoll, A.; Koeberl, C.; Anderson, R. S.; and Ishman, S. E. 2011. The Younger Dryas impact hypothesis: a requiem. Earth-Sci. Rev. 106:247–264.

Redmond, B. G., and Tankersley, K. B. 2005. Evidence of early Paleoindian bone modification and use at the Sheriden Cave site (33WY252), Wyandot County, Ohio. Am. Antiquity 70(3):503–526.

———. 2011. Species response to the theorized Clovis comet impact at Sheriden Cave, Ohio. Curr. Res. Pleistocene 28:141–143.

Reimer, P. J.; Baillie, M. G. L.; Bard, E.; Bayliss, A.; Beck, J. W.; Bertrand, C. J. H.; Blackwell, P. G.; et. al. 2004. IntCal04 terrestrial radiocarbon age calibration, 0–26 ka BP. Radiocarbon 46:1029–1058.

Robinson, G. S.; Burney, L. P.; and Burney, D. A. 2005. Landscape paleoecology and megafaunal extinction in southeastern New York state. Ecol. Monogr. 75:295–315.

Schultz, P. H.; Harris, R. S.; Clemett, S. J.; Thomas-Keprta, K. L.; and Zárate, M. 2014. Preserved flora and organics in impact melt breccias. Geology 42:515–518. doi:10.1130/G35343.1.

Scott, A. C.; Hardiman, M.; Pinter, N.; Anderson, R. S.; Daulton, T. L.; Ejarque, A.; Finch, P.; and Carter-Champion, A. 2017. Interpreting palaeofire evidence from fluvial sediments: a case study from Santa Rosa Island, California, with implications for the Younger Dryas impact hypothesis. J. Quat. Sci. 32(1):35–47.

Scott, A. C.; Pinter, N.; Collinson, M. E.; Hardiman, M.; Anderson, R. S.; Brain, A. P. R.; Smith, S. Y.; Marone, F.; and Stampanoni, M. 2010. Fungus, not comet or catastrophe, accounts for carbonaceous spherules in the Younger Dryas "impact layer." Geophys Res. Lett. 37(14):L14302. doi:10.1029/2010GL043345.

Sharma, M.; Chen, C.; Jackson, B. P.; and Abouchami, W. 2009. High resolution osmium isotopes in deep-sea ferromanganese crusts reveal a large meteorite impact in the central Pacific at 12 ± 4 ka. EOS: Trans. Am. Geophys. Union 90(52), Fall Meeting suppl., abstract PP33B-06.

Stančikaitė, M.; Šinkūnas, P.; Šeirienė, V.; and Kisielienė, D. 2009. Patterns and chronology of the Lateglacial environmental development at Pamerkiai and Kašučiai, Lithuania. Quat. Sci. Rev. 27:127–147.

Stuiver, M., and Reimer, P. J. 1993. Extended ^{14}C database and revised CALIB 3.0 ^{14}C age calibration program. Radiocarbon 35:215–230.

Stuiver, M.; Reimer, P. J.; Bard, E.; Beck, J. W.; Burr, G. S.; Hughen, K. A.; Kromer, B.; McCormac, G.; van der Plicht, J.; and Spurk, M. 1998. INTCAL98 Radiocarbon age calibration, 24,000–0 cal BP. Radiocarbon 40:1041–1083.

Surovell, T. A.; Holliday, V. T.; Gingerich, J. A. M.; Ketron, C.; Haynes, C. V., Jr.; Hilman, I.; Wagner, D. P.; Johnson, E.; and Claeys, P. 2009. An independent evaluation of the Younger Dryas extraterrestrial impact hypothesis. Proc. Natl. Acad. Sci. USA 106:18,155–18,158.

Tankersley, K. B. 1997. Sheriden: a Clovis cave site in eastern North America. Geoarcheology 12(6):713–724.

———. 1999. Sheriden: a stratified Pleistocene-Holocene cave site in the Great Lakes region of North America. *In* Driver, J. C., ed. Zooarchaeology of the Pleistocene/Holocene boundary: proceedings of a symposium held at the 8th Congress of the International Council for Archeo Zoology (ICAZ). BAR Int. Ser. 800, p. 67–75.

———. 2009. Evidence of the Clovis age comet at Sheriden Cave, Ohio. Midwest Chapter of the Friends of Mineralogy Symposium and Field Conference (Oxford, OH, 2009).

Tankersley, K. B.; Ford, K.; McDonald, G.; Genheimer, R.; and Hendricks, R. 1997. Late Pleistocene archaeology of Sheriden Cave, Wyandot County, Ohio. Curr. Res. Pleistocene 14:81–83.

Tankersley, K. B., and Landefeld, C. S. 1998. Geochronology of Sheriden Cave, Ohio: the 1997 field season. Curr. Res. Pleistocene 15:136–138.

Tankersley, K. B., and Redmond, B. 1999*a*. Fluoride/radiocarbon dating of late Pleistocene bone from Sheriden Cave, Ohio. Curr. Res. Pleistocene 16:107–108.

———. 1999*b*. Radiocarbon dating of a projectile point from Sheriden Cave, Ohio. Curr. Res. Pleistocene 16:76–77.

Tankersley, K. B.; Redmond, B. G.; and Grove, T. 2001. Radiocarbon dates associated with a single-beveled bone projectile point from Sheriden Cave, Ohio. Curr. Res. Pleistocene 18:61–63.

Tian, H.; Schryvers, D.; and Claeys, P. 2011. Nanodiamonds do not provide unique evidence for a Younger Dryas impact. Proc. Natl. Acad. Sci. USA 108(1):40–44.

Tinner, W., and Hu, F. S. 2003. Size parameters, size-class distribution and area-number relationship of microscopic charcoal: relevance for fire reconstruction. Holocene 13:499–505.

van der Hammen, T., and van Geel, B. 2008. Charcoal in soils of the Allerød–Younger Dryas transition were the result of natural fires and not necessarily the effect of an extra-terrestrial impact. Neth. J. Geosci. 87(4):359–361.

van Hoesel, A.; Hoek, W. Z.; Pennock, G. M.; and Drury, M. R. 2014. The Younger Dryas impact hypothesis: a critical review. Quat. Sci. Rev. 83:95–114.

van Hoesel, A.; Hoek, W. Z.; van der Plicht, J.; Pennock, G. M.; and Drury, M. R. 2012. Nanodiamonds and wildfire evidence in the Usselo horizon postdate the Allerød–Younger Dryas boundary. Proc. Natl. Acad. Sci. USA 109(2):7648–7653.

Varricchio, D. J.; Raven, R. F.; Wolbach, W. S.; Elsik, W. C.; and Witzke, B. J. 2009. Soot and palynologic analysis of Manson impact-related strata (Upper Cretaceous) of Iowa and South Dakota, USA. Cretac. Res. 30:127–134.

Waters, M. R.; Forman, S.; Stafford, T. W., Jr.; and Foss, J. 2009*a*. Geoarchaeological investigations at the Topper and Big Pine Tree sites, Allendale County, South Carolina. J. Archaeol. Sci. 36(7):1300–1311.

Waters, M. R.; Stafford, T. W., Jr.; Redmond, B. G.; and Tankersley, K. B. 2009*b*. The age of the Paleoindian assemblage at Sheriden Cave, Ohio. Am. Antiquity 74:107–111.

Watson, A. Y., and Valberg, P. 2001. Carbon black and soot: two different substances. AIHAJ 62:218–228.

Watts, W. A. 1979. Late Quaternary vegetation of central Appalachia and the New Jersey coastal plain. Ecol. Monogr. 49(4):427–469.

Weng, C., and Jackson, S. 1999. Late-glacial and Holocene vegetation history and paleoclimate of the Kaibab Plateau, Arizona. Palaeogeogr. Palaeoclimatol. Palaeoecol. 153:179–201.

Wittke, J. H.; Weaver, J. C.; Bunch, T. E.; Kennett, J. P.; Kennett, D. J.; Moore, A. M. T.; Hillman, G. C.; et. al. 2013. Evidence for deposition of 10 million tonnes of impact spherules across four continents 12,800 y ago. Proc. Natl. Acad. Sci. USA 110(23):E2088–E2097.

Wu, Y.; Sharma, M.; LeCompte, M. A.; Demitroff, M.; and Landis, J. 2013. Origin and provenance of spherules and magnetic grains at the Younger Dryas boundary. Proc. Natl. Acad. Sci. USA 110(38):E3557–E3566.